THE FASEB JOURNAL • RESEARCH • www.fasebj.org

Biallelic mutation of human *SLC6A6* encoding the taurine transporter TAUT is linked to early retinal degeneration

Markus N. Preising,[*] Boris Görg,[†] Christoph Friedburg,[*] Natalia Qvartskhava,[†] Birgit S. Budde,[‡] Michele Bonus,[§] Mohammad R. Toliat,[‡] Christopher Pfleger,[§] Janine Altmüller,[‡,¶] Diran Herebian,[#] Mila Beyer,[†] Helge J. Zöllner,[**] Hans-Jörg Wittsack,[††] Jörg Schaper,[††] Dirk Klee,[††] Ulrich Zechner,[‡‡,§§] Peter Nürnberg,[‡,¶,¶¶] Jörg Schipper,[‖‖] Alfons Schnitzler,[**] Holger Gohlke,[§,##] Birgit Lorenz,[*] Dieter Häussinger,[†,1] and Hanno J. Bolz[‖,‡‡,2]

[*]Department of Ophthalmology, Justus-Liebig University Giessen, Giessen, Germany; [†]Department of Gastroenterology, Hepatology, and Infectious Diseases, [#]Department of General Pediatrics, Neonatology, and Pediatric Cardiology, Medical Faculty, [**]Institute of Clinical Neuroscience and Medical Psychology, [††]Department of Diagnostic and Interventional Radiology, and [‖‖]Klinik für Hals-Nasen-Ohren Heilkunde, University Hospital Düsseldorf–Heinrich Heine University Düsseldorf, Düsseldorf, Germany; [‡]Cologne Center for Genomics, [¶]Center for Molecular Medicine Cologne, [‖]Institute of Human Genetics, and [¶¶]Cologne Excellence Cluster on Cellular Stress Responses in Aging-Associated Diseases (CECAD), University of Cologne, Cologne, Germany; [§]Institute for Pharmaceutical and Medicinal Chemistry, Heinrich Heine University Düsseldorf, Düsseldorf, Germany; [‡‡]Senckenberg Centre for Human Genetics, Frankfurt on the Main, Germany; [§§]Institute of Human Genetics, Mainz University, Medical Center, Mainz, Germany; and [##]John von Neumann Institute for Computing (NIC)–Jülich Supercomputing Centre (JSC)–Structural Biochemistry, Institute for Complex Systems (ICS 6), Research Centre Jülich, Jülich, Germany

ABSTRACT: We previously reported that inactivation of the transmembrane taurine transporter (TauT or solute carrier 6a6) causes early retinal degeneration in mice. Compatible with taurine's indispensability for cell volume homeostasis, protein stabilization, cytoprotection, antioxidation, and immuno- and neuromodulation, mice develop multisystemic dysfunctions (hearing loss; liver fibrosis; and behavioral, heart, and skeletal muscle abnormalities) later on. Here, by genetic, cell biologic, *in vivo* ^{1}H–magnetic resonance spectroscopy and molecular dynamics simulation studies, we conducted in-depth characterization of a novel disorder: human TAUT deficiency. Loss of TAUT function due to a homozygous missense mutation caused panretinal degeneration in 2 brothers. TAUT$_{p.A78E}$ still localized in the plasma membrane but is predicted to impact structural stabilization. ^{3}H-taurine uptake by peripheral blood mononuclear cells was reduced by 95%, and taurine levels were severely reduced in plasma, skeletal muscle, and brain. Extraocular dysfunctions were not yet detected, but significantly increased urinary excretion of 8-oxo-7,8-dihydroguanosine indicated generally enhanced (yet clinically unapparent) oxidative stress and RNA oxidation, warranting continuous broad surveillance.—Preising, M. N., Görg, B., Friedburg, C., Qvartskhava, N., Budde, B. S., Bonus, M., Toliat, M. R., Pfleger, C., Altmüller, J., Herebian, D., Beyer, M., Zöllner, H. J., Wittsack, H.-J., Schaper, J., Klee, D., Zechner, U., Nürnberg, P., Schipper, J., Schnitzler, A., Gohlke, H., Lorenz, B., Häussinger, D., Bolz, H. J. Biallelic mutation of human *SLC6A6* encoding the taurine transporter TAUT is linked to early retinal degeneration. FASEB J. 33, 000–000 (2019). www.fasebj.org

KEY WORDS: exome sequencing · homozygosity mapping · consanguinity

ABBREVIATIONS: 8-oxo-Gsn, 8-oxo-7,8-dihydroguanosine; BCVA, best corrected visual acuity; BSA, bovine serum albumin; CAP, controlled attenuation parameter; CNA, Constraint Network Analysis; CRLB, Cramér-Rao lower bound; DAT, *Drosophila melanogaster* sodium-dependent dopamine transporter; EL, extracellular loop; ERG, electroretinogram; ffERG, full-field (Ganzfeld) ERG; FoV, field of view; GCL, ganglion cell layer; GVF, Goldmann visual field; HBD, homozygosity by descent; ID, identifier; INL, inner nuclear layer; LOD, logarithm of the odds; logMAR, logarithm of the minimum angle of resolution; MAF, minor allele frequency; MD, molecular dynamics; mfERG, multifocal ERG; MRS, magnetic resonance spectroscopy; NGS, next-generation sequencing; NPT, isothermal-isobaric; OCT, optical coherence tomography; OS, outer segment; PBMC, peripheral blood mononuclear cell; PDB, Protein Data Bank; RMSD, root-mean-square deviation; SLC, solute carrier; SNP, single-nucleotide polymorphism; SNV, single-nucleotide variant; SR-SIM, superresolution structured illumination microscopy; TAC, Teller acuity card; TAUT, taurine transporter; TE, echo time; TM, transmembrane helix; TR, repetition time; WES, whole-exome sequencing

[1] Correspondence: Department of Gastroenterology, Hepatology, and Infectious Diseases, Universitätsklinikum Düsseldorf, Moorenstr. 5, 40225 Düsseldorf, Germany. E-mail: haeussin@uni-duesseldorf.de

[2] Correspondence: Senckenberg Centre for Human Genetics, Weismüllerstr. 50, 60314 Frankfurt, Germany. E-mail: h.bolz@senckenberg-humangenetik.de

doi: 10.1096/fj.201900914RR

Taurine is the most abundant free amino acid in many mammalian tissues. It can be synthesized endogenously from cysteine, but dietary intake is indispensable for taurine homeostasis. The zwitterionic nature of taurine prevents its passage through lipid layers and allows the sodium-dependent taurine transporter (TAUT), which is encoded by the solute carrier (SLC) 6A6 gene (1), to build up as high as several hundred-fold intra- and extracellular concentration gradients. The biologic functions of taurine are diverse; it serves as an organic osmolyte; contributes to cell volume homeostasis, protein stabilization, and cytoprotection; acts as an antioxidant; and has immuno- and neuromodulatory properties (2–4). Biallelic disruption of the gene coding for TAUT in mice triggered the development of skeletal and heart muscle dysfunction (5), chronic liver disease (6), and auditory and olfactory dysfunction, as well as neurologic abnormalities (4). Whereas these alterations occurred in later life, retinal degeneration with complete loss of vision manifested within 6 wk in these animals (7).

The retina is one of the most taurine-abundant tissues in the body, mainly because of high concentrations in the photoreceptor layer peaking during its formation and remaining high in adulthood, indicating a role for both photoreceptor development and maintenance. TAUT transports nutritional taurine into retinal pigment epithelium cells, which supply it to the photoreceptor cells (8). Nutritional taurine deficiency in cats causes massive photoreceptor degeneration (9), particularly upon light exposure (10), and leads to abnormal electroretinography (ERG) in humans, reversible by intravenous taurine supplementation (11, 12). *SLC6A6* therefore represents a prime candidate for inherited retinal dystrophy in humans.

By genetic, clinical, and functional investigations, we show for the first time that inherited loss of TAUT function severely reduces intracellular taurine levels, the most abundant amino acid in the retina, and causes an atypical panretinal degeneration with loss of outer retina and progressive thickening of inner retinal layers in humans.

We report on 2 boys with early-onset retinal degeneration caused by a homozygous *SLC6A6* mutation. Multisystemic affection (hearing loss; liver fibrosis; and behavioral, heart, and skeletal muscle abnormalities), as seen in *Slc6a6*$^{-/-}$ mice, was not yet observed in the affected siblings reported herein at their young ages. However, increased urinary excretion of 8-oxo-7,8-dihydroguanosine (8-oxo-Gsn), reflecting enhanced oxidative stress and RNA oxidation, may indicate various extraocular dysfunctions at a later age.

MATERIALS AND METHODS

Patients

Samples were obtained with written informed consent from each patient or the patients' parents. All investigations were conducted according to the Declaration of Helsinki, and the study was approved by the institutional review boards of the Ethics Committee of the Justus-Liebig University Giessen (149/07), the University Hospital of Cologne, and the Heinrich Heine University Düsseldorf (Study no. 5350).

Ophthalmologic examinations

The patients underwent age-appropriate tests of best corrected visual acuity (BCVA) using Teller acuity cards (TACs), a Lea test, and Landolt ring charts. BCVA was transferred to the negative decadic logarithm of the minimum angle of resolution (logMAR) for reporting. Objective refraction was measured with an A7000B autorefractor (Topcon, Tokyo, Japan), and color vision was tested with a saturated Lanthony Panel D15 test.

Morphologic data were recorded by fundus photography using a Zeiss FF450 Camera and a Clarus 500 ultra-wide field fundus camera (Carl Zeiss Oberkochen, Germany).

Spectral domain optical coherence tomography (OCT) scans were recorded on a Spectralis HRA unit (Heidelberg Engineering, Heidelberg, Germany) with at least single-line scans (B-scan) covering the optic nerve head and the macula. A B-scan consisted of 1536 A-scans. An infrared fundus image accompanied each OCT scan to locate the scan for further evaluation. A-scans were extracted from the B-scans by DiOCTA software (13).

Kinetic Goldmann perimetry (Haag-Streit, Köniz, Switzerland) completed the basic set of examinations. Finger perimetry estimated visual fields at insufficient capacity for Goldmann visual field (GVF) testing.

Ganzfeld ERGs (ffERGs) were recorded on an Espion Unit (Diagnosys, Lowell, MA), and multifocal ERG (mfERG) was recorded on a Veris Science 5.1.D252 (EDI, Cincinnati, OH, USA) with an FMS II stimulator (microdisplay md75) with integrated fundus camera. All electrophysiological recordings were performed according to International Society for Clinical Electrophysiology of Vision standards (14, 15).

Auditory and olfactory assessment

To analyze the inner ear function, 1 subjective hearing test (pure tone audiogram) was performed at the frequencies of 250, 500, 1000, 1500, 2000, 3000, 4000, 6000, and 8000 Hz, and 1 objective hearing test (distortion product otoacoustic emissions) as control of plausibility was performed at the stimulation frequencies of 1000, 1400, 2000, 2800, 4000, 6000, and 8000 Hz.

For the olfactory screening, we used 7 standardized items of the Sniffin' test (Sniffin' Sticks; Sense Trading, Winschoten, The Netherlands). A total of 7 common odorants were tested: orange, leather, cinnamon, peppermint, banana, lemon, and vinegar. The stick without the cap was positioned 2 cm from the nose and presented for 3–4 s, and the patient was asked to sniff. An interval of $\geq$30 s between each stick presentation is recommended to prevent olfactory adaptation. We evaluated odor familiarity and identifiability. Both patients underwent ear, nose, and throat examination of the upper airways.

Additional clinical examinations

Patients underwent physical examination, abdominal sonography, FibroScan (Echosens, Waltham, MA, USA), controlled attenuation parameter (CAP) determination, electrocardiography, and routine laboratory tests.

Genome-wide linkage analysis

Genome-wide genotyping was performed with samples of both affected brothers and their parents using the Axiom Precision Medicine Research Array (Thermo Fisher Scientific, Waltham, MA, USA). Genotypes were called by the Axiom Analysis Suite v4.0 (Thermo Fisher Scientific). Subsequent data handling was performed using the graphical user interface Alohomora (16).

Relationship errors were identified by the program Graphical Relationship Representation (17). The program PedCheck was applied to find Mendelian errors (18), and data for single-nucleotide polymorphisms (SNPs) with such errors were removed from the data set. Non-Mendelian errors were identified by using the program Multipotent Engine for Rapid Likelihood Inference (MERLIN) (19), and unlikely genotypes for related samples were deleted. Linkage analysis was performed assuming autosomal recessive inheritance, full penetrance, consanguinity, and a disease allele frequency of 0.0001. Multipoint, logarithm of the odds (LOD) scores were calculated using MERLIN. Haplotypes were reconstructed with MERLIN and presented graphically with HaploPainter (20). The 2-yr-old sister of the patients was not presented to us initially and was genotyped for the *SLC6A6* variant in the course of segregation analysis.

Next-generation sequencing

Targeted next-generation sequencing (NGS) was carried out for the index patient (II:1). Library preparation was performed using the Kapa HyperPlus Kit (Roche, Basel, Switzerland) followed by enrichment with Integrated DNA Technologies xGen Inherited Diseases Panel v1.0 (Integrated DNA Technologies, Coralville, IA, USA) covering genomic regions containing genes and SNPs associated with inherited diseases. In short, 100 ng of genomic DNA were fragmented to a peak size of 150–200 bp using Kapa Frag enzyme (Roche). The fragmented genomic DNA was end repaired, A tailed, ligated to single-indexed adapters, and PCR amplified according to the manufacturer's instructions. PCR reactions were purified using Kapa Pure Beads (Roche). For target capture, 500 ng of pooled libraries (8 libraries per pool) were hybridized to biotinylated oligonucleotides at 65°C for 4 h. The captured libraries were pulled down using Dynabeads M-270 Streptavidin (Thermo Fisher Scientific). A postcapture PCR was carried out to amplify the captured libraries and add the barcode sequences for multiplex sequencing for 12 cycles. Subsequently, amplified libraries were cleaned with Agencourt AMPure XP Beads (Beckman Coulter, Brea, CA, USA). Each captured library was quantified and validated using a Qubit fluorometer (Thermo Fisher Scientific) and Agilent Bioanalyzer high sensitivity chips (Agilent Technologies, Santa Clara, CA, USA). The pooled libraries were paired-end sequenced on an Illumina NextSeq 500 system (Illumina, San Diego, CA, USA). Read mapping against the hg19 human reference genome, variant calling, annotation, and filtering against 1000 genomes and Exome Aggregation Consortium (ExAC; *http://exac.broadinstitute.org/*) were performed for 138 genes known to be associated with inherited retinal dystrophies (autosomal dominant and autosomal recessive retinitis pigmentosa; X-linked

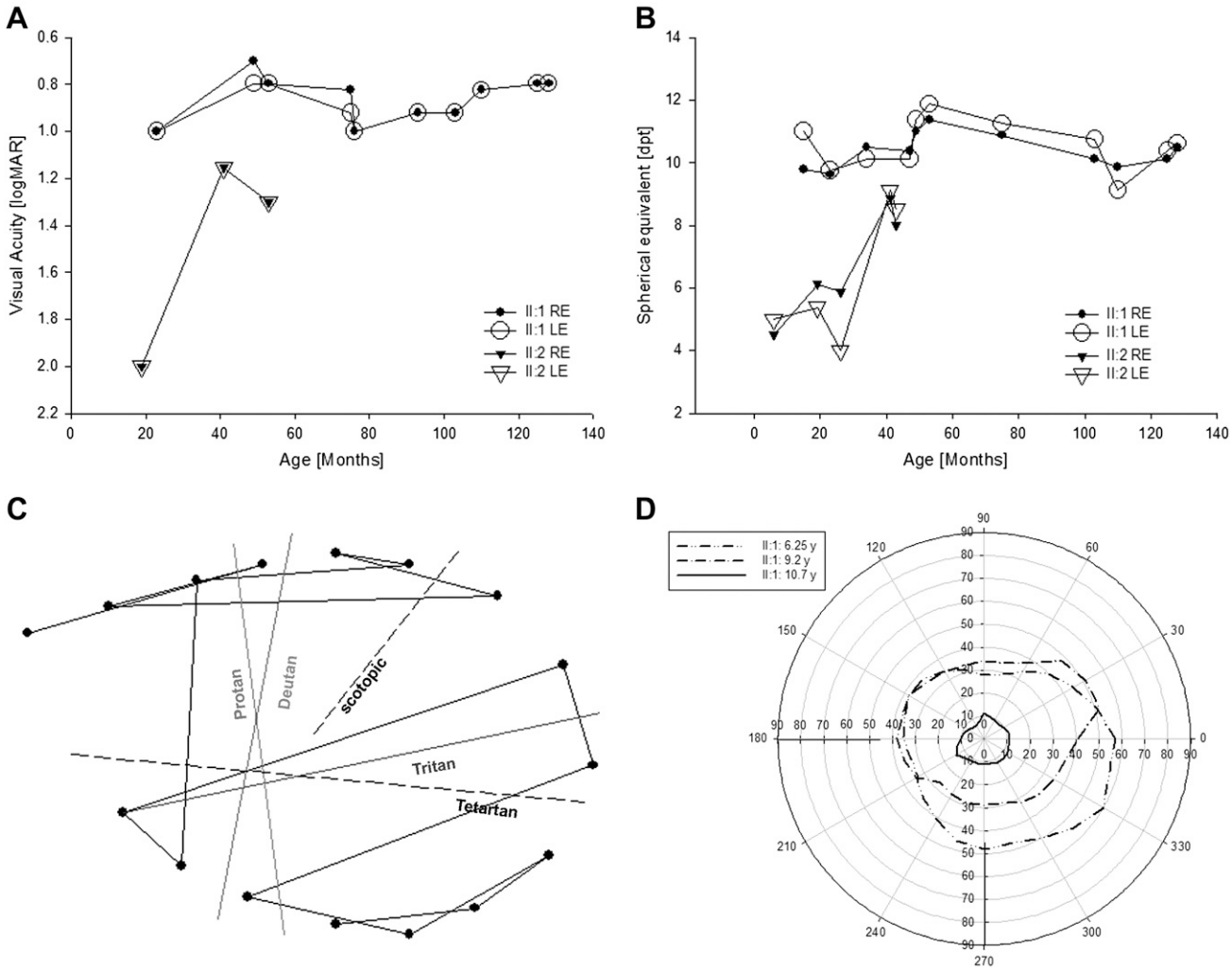

Figure 1. Examination of visual function reveals severe impairment of rods and cones. *A*) Visual acuity in patients II:1 and II:2 reveals severely reduced but stable vision. *B*) Refraction in both patients is highly hyperopic. *C*) Color vision testing in patient II:1 at 10.7 yr of age using the saturated Lanthony Panel D15 test indicated a more pronounced blue color vision reduction (left eye shown). *D*) Bilateral GVF testing in patient II:1 shows narrowing in progression. dpt, diopters; LE, left eye; RE, right eye.

TABLE 1. *Longitudinal data of patients with mutations in SLC6A6*

Patient	Age (yr)	BCVA Test: RE/LE (logMAR)	Refraction	GVF	OCT	Fundus	ERG	Neuro-opthalmology
II:1	1.25		RE: +9.5/−2.0/0°; LE: +8.75/−2.0/10°			M: noa[a]		nys
	1.9	TAC: 1.0/1.0	RE: +10.25/−2.0/1°; LE: +10.25/−2.5/170°					
	2.4		RE: +8.75/−2.0/8°; LE: +8.5/−2.25/166°			M: irregular, pale[a]		
	2.8		RE: +10.75/−2.25/5°; LE: +10.25/−3.0/174°			M: no MR[a]; P: noa[a]		
	4.1	LT: 0.70/0.80	RE: +9.0/−2.25/12°; LE: +9.0/–2.75/172°					
	4.4	LT: 0.80/0.80	RE: +10.25/−2.25/5°; LE: +9.75/−2.5/173°			FP: noa[a]; IR: mottled fundus no macular structure		
	6.25	LR: 0.80/0.92	RE: +10.75/−2.25/2°; LE: +10/−2.75/174°	bin; V/4e: ~48% o.n.	M: reduced thickness and lost stratification of ELM-OS; P: ELM-OS missing (Fig. 2*B, H*)	FP: M to P: noa[a]		
	6.3	LR: 1.0/1.0	RE: +10.0/−2.5/12°; LE: +9.5/−2.75/173°			ONH: pale M: noa[a]	ffERG: scot + phot bt mfERG: ncp	nys + exo
	7.75	LR: 0.92/0.92		bin; I/4e: 10°; III/4e: 30–60°		M-P: noa[a]		
	8.6	LR: 0.92/0.92	RE: +9.5/−2.5/179°; LE: +9.0/−2.25/176°					
	9.2	LR: 0.82/0.82	RE: +8.0/−2.25/3°; LE: +8.5/−2.75/173	bin; V/4e: ~43% o.n.				
	10.4	LR: 0.80/0.80	RE: +9.25/−2.25/5°; LE: +8.75/−2.75/175°	bin;V/4e: ~19% o.n.				
	10.7	LR: 0.80/0.80	RE: +9.5/−2.25/180°; LE: +9.0/−3.0/175°	RE/LE; III/4e: 3°; V/4e: 10–15°∂ ~12% o.n.	M: reduced thickness and lost stratification of ELM-OS; P: ELM-OS missing (Fig. 2*C, H*)	FP: M: no MR; P: pigment irregularities		Panel D15: blue cone deficiency
	11.25				Fig. 2*D, H*	FP: M: paramacular reflexes and irregular borders; P: pigment irregularities; IR: mottled fundus, no macular structure, attenuated vessels (Fig. 2*A–G*)		

(*continued on next page*)

TABLE 1. (*continued*)

Patient	Age (yr)	BCVA Test: RE/LE (logMAR)	Refraction	GVF	OCT	Fundus	ERG	Neuro-opthalmology
	11.4				M: reduced thickness and lost stratification of ELM-OS regressed, macular edema in INL thickened GCL, and irregular RNFL; P: ELM-OS missing (Fig. 2*E*)			
II:2	0.5	Fixation				noa[a]		nys
	1.6	TAC: 2.0/2.0	RE: +5.0/−0.75/4°; LE: +5.5/−1.25/2°			Noa[a]		
	2.2		RE: +3.5/−1.0/24°; LE: +5.0/−1.75/10°			noa[a]		
	3.4	TAC: 1.15/1.15	RE: +8.25/−1.75/20°; LE: +8.25/−1.25/170°			noa*		
	3.6		RE: +7.75/−1.5/10°; LE: +7.25/−1.5/162°	PF: bin; ↔ 40°, ↕ 20–25°		FP: M-P: small flecks, dull fundus		
	4.25	LH: 1.3/1.3			M: reduced thickness and lost stratification of ELM-OS, ME in INL, reduced thickened GCL, and irregular RNFL; P: ELM-OS missing (Fig. 2*F*, *H*)	IR: mottled fundus and dark ring surrounding fovea		

[a]Limited by nystagmus and cooperativity. ↔, horizontal; ↕, vertical; bin, binocular; bt, below threshold; ELM, external limiting membrane; exo, exotropia; FP, fundus photography; IR, infrared fundus photography; LE, left eye; LH, Lea Hyvarinen; LR, Landolt ring; M, macula; ME, macular edema; MR, macular reflex; ncp, no correlated potentials; noa, no obvious alterations; nys, nystagmus; o.n., of normal; ONH, optic nerve head; P, periphery; PF, finger perimetry; phot, photopic; RE, right eye; RNFL, retinal nerve fiber layer; scot, scotopic; TAC, Teller acuity cards.

retinitis pigmentosa; Leber congenital amaurosis; cone, cone-rod, and macular dystrophies; and congenital stationary nightblindness) with the SeqNext module of the SeqPilot software (JSI Medical Systems, Costa Mesa, CA, USA). The cutoff for the maximum minor allele frequency (MAF) was set to 1%. Variants were checked for their presence in the disease-specific variant databases ClinVar (*http://www.ncbi.nlm.nih.gov/clinvar/*) and Human Gene Mutation Database (HGMD; *http://www.hgmd.cf.ac.uk/ac/index.php*). Nonsense, frameshift, and canonical splice site variants were regarded as likely pathogenic. Single-nucleotide variants (SNVs) were assessed using scores from the pathogenicity prediction algorithms DANN (deleterious annotation of genetic variants using neural networks), MutationTaster2, FATHMM (Functional Analysis Through Hidden Markov Models), FATHMM-MKL (Functional Analysis Through Hidden Markov Models - Multiple Kernel L\earning), MetaSVM (Meta Support Vector Machine), MetaLR (Meta Logistic Regression), LRT (Likelihood Ratio Test), MutationAssessor, SIFT (Sorts Intolerant From Tolerant substitutions), and PROVEAN (Protein Variation Effect Analyzer) as well as conservation scores from GERP++ (Genomic Evolutionary Rate Profiling++), phyloP20way (phylogenetic P-values 20way), phyloP100way (phylogenetic P-values 100way), SiPhy29way (Site-specific PHYlogenetic analysis 29way), fitCons-gm (fitness Consequence GM12878), phastCons20way (PHylogenetic Analysis with Space/Time models conservation 20way), and phastCons100way (PHylogenetic Analysis with Space/Time models conservation 100way) compiled by the Database of Human Nonsynonymous SNPs and Their Functional Predictions (dbNSFP) (9). Whole-exome sequencing (WES) was conducted with the DNA of the index patient after Agilent SureSelect v.6 exome target capture on an Illumina HiSeq 4000 sequencing instrument, the standard protocol SureSelectXT Automated Target Enrichment for Illumina paired-end multiplexed sequencing, the Agilent SureSelect v6 exome target capture, and the Agilent Bravo automated liquid handling platform. After validation (2200 TapeStation; Agilent Technologies) and quantification (Qubit System; Thermo Fisher Scientific), the exome library was pooled and sequenced on an Illumina HiSeq 4000 sequencing instrument using a paired-end 2 × 75 bp protocol and an allocation of 1 pool with 6 exomes per lane. A local pipeline (21) and interface was used (Varbank 2.0; *https://varbank.ccg.uni-koeln.de/varbank2/*) as previously described in refs. 22 and 23). We searched the ExAC and Genome Aggregation Database (gnomAD; *https://gnomad.broadinstitute.org/*) databases (24) (as of November 2018) for homozygous candidate variants identified by targeted NGS and WES in our index patient. PCR amplification of *SLC6A6* exon 4 and subsequent Sanger sequencing was carried out for segregation analysis in both patients and their parents.

Isolation of human peripheral blood mononuclear cells

Peripheral blood was subjected to BD Vacutainer Mononuclear Cell Preparation Tubes (BD Biosciences, San Jose, CA, USA) and mixed by gentle inversion several times to ensure a homogeneous suspension. The tubes were centrifuged at 1650 *g* for 20 min at room temperature. The plasma and peripheral blood mononuclear cell (PBMC) layer were gently collected and pipetted into a sterile 50-ml tube. Then, tubes were filled with HBSS (Harvard Bioscience, Holliston, MA, USA) to a final volume of 50 ml and centrifuged at 300 *g* for 10 min at 4°C. The supernatant was aspirated carefully and discarded. The pellet was resuspended in 50 ml HBSS and centrifuged for 10 min at 300 *g*. This procedure was repeated twice. Finally, cells were resuspended in 10 ml Roswell Park Memorial Institute (RPMI) 1640 medium (Thermo Fisher Scientific) containing 25 mM 4-(2-hydroxyethyl)-1-piperazineethanesulfonic acid. The total amount of cells was determined by manual counting using a glass hemocytometer. Measurements were performed using ~20–30 Mio/ml PBMCs.

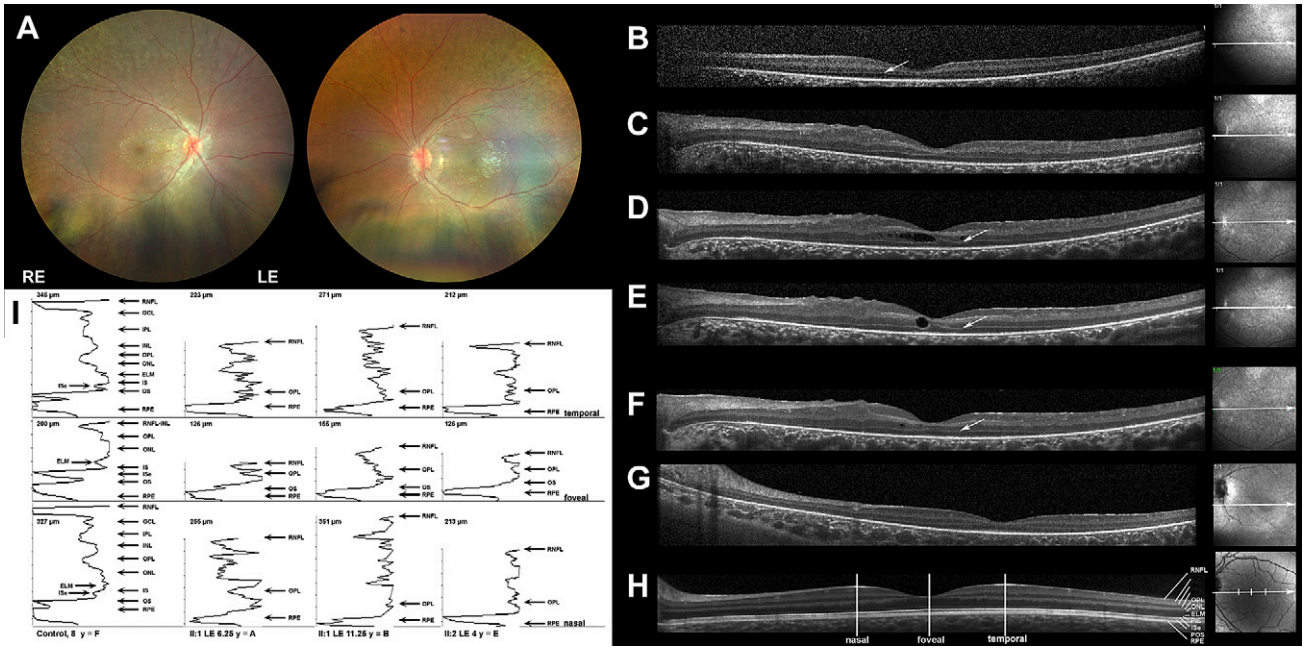

Figure 2. OCT reveals photoreceptor and retinal ganglion cell affection. *A*) Ultra-wide field fundus photographs of patient II:1 at 11.4 yr of age (both eyes). OCT recordings in patient II:1 at the age of 6.25 (*B*), 10.7 (*C*), 11.25 (*D*), 11.4 (*E*), and 11.5 (*F*) yr. *G*) Patient II:2 at the age of 4 yr. *H*) Age-similar healthy control (8 yr). Black arrowhead indicates the OPL. *I*) A-scan analysis from OCT recordings evaluates retinal stratification at the indicated position in the B-scan of the age-similar control (black bars in *F*). Patient II:1 (left eye at 6, 25, and 11.25 yr of age) and II:2 (left eye at 4 yr of age) compared with control (left eye and 8 yr of age). ELM, external limiting membrane; IPL, inner plexiform layer; IS, inner segment; ISe, inner segment ellipsoid; LE, left eye; ONL, outer nuclear layer; OPL, outer plexiform layer; PIS, photoreceptor inner segment; POS, photoreceptor outer segment; RE, right eye; RNFL, retinal nerve fiber layer; RPE, retinal pigment epithelium.

TABLE 2. *Liver stiffness (FibroScan) and CAP*

Subject	Transient elastography (kPa)	CAP (db/m)
Father (heterozygous)	2.3	214
Mother (heterozygous)	2.7	164
Patient 1 (homozygous)	4.6	249
Patient 2 (homozygous)	4.1	218

In both patients, there was no evidence for fibrosis or cirrhosis and no signs of significant liver steatosis.

Uptake of taurine by human PBMCs

For measuring taurine uptake, isolated human PBMCs were incubated in Roswell Park Memorial Institute 1640 medium supplemented with 10 μM taurine and 5.6 nM [^{3}H] taurine (0.1 μCi/ml; PerkinElmer, Waltham, MA, USA) for the time periods indicated (0, 60, and 180 min) at 37°C. At the end of the incubation period, cell suspensions were centrifuged at 1650 *g* for 10 min at 4°C, and supernatants were collected for [^{3}H] taurine measurement. The cell pellets were carefully resuspended in ice-cold PBS (PAN Biotech, Aidenbach, Germany) and washed 3 times by centrifugation (1650 g for 10 min at 4°C). Thereafter, the pellets were collected in 1 ml PBS containing 1% SDS (MilliporeSigma, Burlington, MA, USA) and 0.1% benzonase (Merck, Kenilworth, NJ, USA). [^{3}H] taurine content in the supernatants and cell lysates were measured by a scintillation counter and are expressed as percentage of total [^{3}H] taurine (medium without cells) normalized to the total number of cells incubated.

TAUT immunofluorescence analysis

TAUT expression in PBMCs was analyzed by immunofluorescence and superresolution structured illumination microscopy (SR-SIM) as previously described by Görg *et al*. (25). Isolated PBMCs were fixed for 10 min in freshly prepared ice-cold paraformaldehyde (28908, TG2609191; Thermo Fisher Scientific). Cells were washed thrice with ice-cold PBS (P04-35500, 4921117; PAN Biotech) before cells were permeabilized and blocked in PBS containing 0.1% Triton X-100 (T9284-500 ml, SLBL8213V; MilliporeSigma) and 5% bovine serum albumin (BSA) fraction V (10735108001, 32123400; Roche). At the end of the incubation period, cells were washed in PBS + 5% BSA and incubated for 1.5 h at room temperature with pAb against rabbit anti-Slc6a6 (1:50, ab236898, GR3244338-1; Abcam, Cambridge, United Kingdom) in PBS + 5% BSA. Unbound antibodies were removed by washing the cells twice in PBS + 5% BSA before cells were incubated with cyanine 3–conjugated donkey anti-rabbit IgG (1:200, 711-165-152, 139288; dianova, Hamburg, Germany), Phalloidin-FITC (1:100, P5282, SLBN4831V; MilliporeSigma), and Hoechst 34580 (1:5.000, H21486, l1679155; Roche). Cells were washed thrice with PBS and mounted on Ibidi μ-dishes (Ø35 mm, high, glass bottom; 81158, 108060515; Ibidi, Gräfelfing, Germany) in Fluoromount-G (0100-01, H0318-V198; Biozol, Eching, Germany).

μ-Dishes were mounted on the Elyra PS.1 microscope and imaged using an α Plan-Fluar ×100/1.45 M27 oil-immersion objective and Immersol 518F immersion fluid (Carl Zeiss). SR-SIM images were processed using Zen software (2.3, SP1, black, 64bit, v.14.0.0.0; Carl Zeiss) according to the manufacturer's instruction.

Amino acid analysis

The amino acid analyzer Biochrom 30+ (Laborservice Onken, Gründau, Germany) was used for separation and detection of amino acids, biogene amines, and taurine in serum and urine samples. The method of the system is based on ion exchange chromatography with Ninhydrin post column derivatization.

Determination of 8-oxo-Gsn

The concentration of 8-oxo-Gsn in urine samples was determined by liquid chromatography coupled to tandem mass spectrometry. Urine samples were collected as single-spot samples, and the concentration was adjusted by creatinine concentration. All samples were run in duplicate. The system consisted of an UPLC-I class (Waters, Milford, MA, USA) coupled to a Xevo TQ-S triple quadrupole mass spectrometer (Waters). Electrospray ionization was performed in the positive ionization mode. Detection of 8-oxo-Gsn was performed in multiple-reaction monitoring mode with the following mass transitions: 300.1 > 168 and 300.1 > 140 *m/z* (26).

Bile acid analysis

Bile acids and their glycine- and taurine-conjugated derivatives were analyzed by ultraperformance liquid chromatography–tandem mass spectrometry. The system consisted of an Acquity UPLC-I Class (Waters) coupled to a Waters Xevo-TQS tandem mass spectrometer equipped with an electrospray ionization

TABLE 3. *Serum taurine levels and taurine and 8-oxo-Gsn excretion into urine in the reported family*

Subject	Serum taurine level (μM)	Urinary taurine, mmol/mol creatinine	Urinary 8-oxo-Gsn, μmol/mol creatinine
Father (42 yr old; heterozygous)	110 (42–155)	35 (16–180)	7.7 (1.9 ± 0.54)
Mother (32 yr old; heterozygous)	74 (41–197)	162 (16–180)	5.7 (1.6 ± 0.5)
Patient II:1 (11 yr old; homozygous)	4 (42–155)	120 (18–230)	20.5 (1.48 ± 0.61)
Patient II:2 (4 yr old; homozygous)	4 (90–133)	196 (17–203)	22.1 (4.76 ± 1.45)
Daughter (2 yr old; wild type)	128 (30–133)	116 (13–200)	1.4 (4.76 ± 1.45)

The given reference values are age adjusted. Normal ranges are indicated in parentheses. Reference values for age-dependent 8-oxo-Gsn excretion into urine in healthy individuals are from Gan *et al.* (26). Norm, normal.

TABLE 4. *Bile acid concentration in serum of patient II:1 (11 yr old)*

Bile	Serum level (μM)	Reference (μM)
TCA	0.02	0–0.18
TCDCA	0.01	0–0.273
TDCA	0.01	0–0.141
TLCA	0.00	0
TUDCA	0.01	0
GCA	0.04	0.03–0.815
GCDCA	0.06	0.057–2.018
GCDA	0.04	0–0.59
GLCA	0.00	0
GUDCA	0.07	0–0.284
CA	0.05	0–3.344
CDCA	0.19	0.002–0.516
DCA	0.54	0.003–0.516
LCA	0.00	0.003–0.594
UDCA	0.06	0–0.368

CA, cholic acid; CDCA, chenodesoxycholic acid; DCA, desoxycholic acid; GCA, glycocholic acid; GCDCA, glycochenodeocycholic acid; GDCA, glycodesoxycholic acid; GLCA, glycolithocholic acid; GUDCA, glycoursodesoxycholic acid; LCA, lithocholic acid; TCA, taurocholic acid; TCDCA, taurochenodeoxycholic acid; TDCA, taurodesoxycholic acid; TUDCA, tauroursodesoxycholic acid; TLCA, taurolithocholic acid; UDCA, ursodesoxycholic acid.

source in the negative ion mode. Data were collected in the multiple-reaction monitoring mode (27).

Magnetic resonance and magnetic resonance spectroscopy measurements

All magnetic resonance investigations were performed on a clinical whole-body 1.5 T MRI (Siemens Magnetom Avanto fit; Siemens Munich, Germany) using a 20-channel head coil to receive the brain spectra, an 18-channel surface coil to receive the muscle spectrum, and the internal body coil for transmitting. point resolved spectroscopy (PRESS) metabolite spectra (echo time (TE)/repetition time (TR) 30/2000 ms, number of expectations (NEX) 128, volume 8 ml, total acquisition time 4:15) and unsuppressed water reference (NEX 8, total acquisition time 0: 34) were acquired in the basal ganglia, the parietal white matter, and the right upper leg muscle.

T2-weighted brain MRI [turbo spin echo (TSE) axial TE/TR 106/5600 ms, turbo factor 18, field of view (FoV) 229 × 208 mm, matrix size 384 × 348, slice thickness 5 mm, gap 0.5 mm, total acquisition time 1:46], liquor suppressed (TSE coronal, TE/TR/ inversion time (TI) 107/8500/2440 ms, turbo factor = 15, slice thickness 0.5 mm, gap 0.5 mm, FoV 230 × 172 mm, matrix size 320 × 240, total acquisition time 3:06), and T1 weighted (3-dimensional magnetization-prepared rapid acquisition with gradient echo sagittal, TE/TR/TI 3.31/1700/1100 ms, FoV 190 × 235 mm, matrix size 312 × 384, 1.25-mm slice thickness, total acquisition time 2:15) was performed prior to the magnetic resonance spectroscopy (MRS). A total of 3 orthogonal T1-weighted gradient echo localizers (TE/TR 6/20 ms, FoV 230 × 230 mm, matrix size 256 × 256, 5-mm slice thickness, gap 6 mm, total acquisition time 2:54) were conducted in the muscle. A healthy control (male, 26 yr old) was measured with the same MRS protocol. The imaging included only the T1-weighted sequences from the patient's protocol.

Metabolite quantification was performed with LCModel v6.3 (28). The muscle basis set was simulated by LCModel, and the basis set for the brain was imported from Tarquin (29). All concentrations were calculated with respect to total creatine. Creatine:water ratios were calculated to control for possible changes in the total creatine.

Molecular dynamics simulations and rigidity analysis of wild-type TAUT and the p.A78E variant

A structural model of human TAUT was generated by comparative modeling based on the crystal structure of the *Drosophila melanogaster* sodium-dependent dopamine transporter (DAT) (30). The structural model of the p.A78E mutant was generated using the mutagenesis functionality in PyMOL (Schrödinger, New York, NY, USA). The wild-type TAUT and p.A78E variant structures were embedded into a membrane bilayer resembling the composition of fibroblasts and solvated with transferable intermolecular potential with 3 points (TIP3P) water (31). After thermalization, molecular dynamics (MD) simulations were carried out using the mixed precision graphics processing unit implementation in the Amber 18 package (32, 33). For both the wild-type TAUT and the p.A78E variant, 5 isothermal-isobaric (NPT)-MD simulations of 1 μs length were carried out, resulting in an aggregate simulation time of 10 μs. Rigidity analysis was performed with the Constraint Network Analysis (CNA) software package (34) on conformational ensembles extracted from the MD trajectories. In order to detect altered stability characteristics due to the p.A78E mutation, a linear response approximation was applied to obtain a per-residue decomposition of the free energy associated with the change in biomolecular stability due to the mutated residue (see rigidity analysis; Eq. 4) (34, 35).

Homology modeling and system setup

A structural model of human TAUT [UniProt accession identifier (ID): P31641] was generated by comparative modeling using the SWISS-MODEL server (36) based on the crystal structure of DAT [Protein Data Bank (PDB) ID: 4M48 (30); sequence identity: ~48%, sequence coverage: ~86%], which belongs to the solute carrier 6 family of transporters (as does TAUT). This structure shows DAT in a nortriptyline-bound, outward-open conformation. Model quality was evaluated with the MolProbity server (37), resulting in a MolProbity score of 1.96, which indicates a geometrically well-defined structure, the accuracy of which is expected to be close to the experimental uncertainty in the transmembrane region (38). The structural model of the p.A78E variant was generated using the mutagenesis functionality in PyMOL.

TABLE 5. *Bile acid concentration in serum of patient II:2 (4 yr old)*

Bile	Serum level (μM)	Reference (μM)
TCA	0.04	0–0.18
TCDCA	0.1	0–0.273
TDCA	0.04	0–0.141
TLCA	0.00	0
TUDCA	0.01	0
GCA	0.58	0.03–0.815
GCDCA	0.63	0.057–2.018
GCDA	0.21	0–0.59
GLCA	0.03	0
GUDCA	0.33	0–0.284
CA	0.01	0–3.344
CDCA	0.03	0.002–0.516
DCA	0.24	0.003–0.516
LCA	0.00	0.003–0.594
UDCA	0.03	0–0.368

CA, cholic acid; CDCA, chenodesoxycholic acid; DCA, desoxycholic acid; GCA, glycocholic acid; GCDCA, glycochenodeocycholic acid; GDCA, glycodesoxycholic acid; GLCA, glycolithocholic acid; GUDCA, glycoursodesoxycholic acid; LCA, lithocholic acid; TCA, taurocholic acid; TCDCA, taurochenodeoxycholic acid; TDCA, taurodesoxycholic acid; TLCA, taurolithocholic acid; TUDCA, tauroursodesoxycholic acid; UDCA, ursodesoxycholic acid.

TABLE 6. *Plasma amino acid levels found in patient II:1 and age-adjusted reference values (11 yr old)*

Plasma amino acid	Amount (μM)	Reference (μM)
Taurine	5	42–155
Asparagine	18	<25
Hydroxyproline	27	<28
Threonine	156	87–171
Serine	134	100–171
Asparagine	62	52–108
Glutamic acid	18	16–75
Glutamine	541	406–794
Proline	200	103–266
Glycine	214	150–325
Alanine	428	232–494
Citrulline	26	17–42
α-Aminobutyric acid	13	<36
Valine	211	147–260
Methionine	23	14–29
Isoleucine	64	41–85
Leucine	115	82–162
Tyrosine	76	44–81
Phenylalanine	55	40–64
Histidine	69	52–100
Ornithine	58	39–96
Lysine	194	113–196

From an overlay of the structural models with the leucine- and sodium-bound structure of the *Aquifex aeolicus* leucine transporter ($LeuT_{Aa}$) [PDB ID: 2A65 (39)], which shows $LeuT_{Aa}$ in the occluded conformation, the potential binding sites of taurine and Na^+ in TAUT were inferred.

The wild-type TAUT and p.A78E variant structures were embedded into a membrane bilayer resembling the composition of fibroblasts (55.4% 1-palmitoyl-2-oleoyl-*sn*-glycero-3-phosphocholine, 16.1% 1-palmitoyl-2-oleoyl-*sn*-glycero-3-phosphoethanolamine; 13.0% cholesterol; 7.6% 1-palmitoyl-2-oleoyl-*sn*-glycero-3-phosphoglycerol; 6.4% 1-palmitoyl-2-oleoyl-*sn*-glycero-3-phosphoserine; 1.5% 1-palmitoyl-2-oleoyl-*sn*-glycero-3-phosphatidic acid) using Chemistry at Harvard Macromolecular Mechanics–Graphical User Interface (CHARMM-GUI; *http://www.charmm-gui.org/*) (40, 41) and solvated with TIP3P water (31) such that the minimum thickness of the water slab on top of and below the protein/membrane system was 25 Å. A total of 154 mM NaCl was added to the system.

MD simulations: general settings

MD simulations were carried out using the mixed precision graphics processing unit implementation in the Amber 18 package (32, 33). A time step of 2 fs was used for integration, and the Langevin thermostat (42, 43) was used for temperature control, with a collision frequency of $\gamma = 2.0\ ps^{-1}$ and a target temperature of $T = 300$ K. Covalent bonds involving hydrogen atoms were constrained using the SHAKE algorithm (44). The Particle Mesh Ewald (45) method was used to estimate long-range electrostatic interactions, and a cutoff of 10 Å was used for short-range electrostatics and van der Waals forces.

MD simulations: equilibration protocol

The initial structures were energy minimized for 2500 steps using the steepest descent algorithm, followed by 2500 steps of minimization with the conjugate gradient algorithm; during this procedure, all protein and membrane atoms were restrained to their initial positions by harmonic restraints with a force constant of 10.0 kcal/mol $Å^{-2}$. This step was first repeated with the force constant of the harmonic restraints lowered to 5.0 kcal/mol $Å^{-2}$, then repeated with the restraints removed from the lipid atoms and, finally, repeated without restraints. After the final minimization step, the root-mean-square deviation (RMSD) of the atomic positions of the backbone atoms was ≤0.5 Å for all systems with respect to the initial structure. 25 ps of canonical (NVT)-MD (*i.e.*, at constant particle number, volume, and temperature; protein restrained; force constant: 2.5 kcal/mol $Å^{-2}$) were performed while heating the system from 0 to 300 K. 1775 ps of NPT-MD (*i.e.*, at constant particle number, pressure, and temperature; protein restrained; force constant: 2.5 kcal/mol $Å^{-2}$) were performed for density adaptation. After removing the restraints, additional 3200 ps of NPT-MD were performed.

MD simulations: production protocol

For both the wild-type and the p.A78E variant, 5 NPT-MD simulations of 1 μs length were carried out, resulting in an aggregate simulation time of 10 μs. The length of the MD simulations surpasses comparable previous ones on neurotransmitter sodium symporters by ≥1 order of magnitude (46, 47) and is ≥10-fold longer than the relaxation time of fluctuations of the membrane area (48), thus allowing for the investigation of potential adaptations of the membrane structure due to the mutation. Coordinates for analysis and postprocessing were saved every 20 ps. The performed unbiased microsecond-long MD simulations at the atomistic level in explicit solvent and an explicit lipid bilayer are currently the most accurate way to computationally explore structure and dynamics of transmembrane proteins (49). We used established parameterizations for the solvent (31), lipids (50), and proteins (51), which we had also applied successfully in other transmembrane protein simulations (52, 53). We performed quintuplicate MD simulations for each system, which allows probing for the influence of the starting conditions and helps overcoming the sampling challenge (54).

MD simulations: postprocessing and data analysis

Postprocessing and analysis of the MD trajectories was performed with CPPTRAJ (55) as implemented in AmberTools17.

TABLE 7. *Plasma amino acid levels found in patient II:2 and age-adjusted reference values (4 yr old)*

Plasma amino acid	Amount (μM)	Reference (μM)
Taurine	5	30–133
Asparagine	13	<20
Hydroxyproline	20	<23
Threonine	90	43–130
Serine	116	70–163
Asparagine	47	37–133
Glutamic acid	21	23–97
Glutamine	476	371–737
Proline	174	76–292
Glycine	189	138–357
Alanine	340	162–517
Citrulline	26	15–38
α-Aminobutyric acid	13	<37
Valine	155	114–286
Methionine	12	<28
Isoleucine	41	32–94
Leucine	83	61–162
Tyrosine	71	33–90
Phenylalanine	52	33–64
Histidine	56	47–78
Ornithine	38	25–84
Lysine	109	78–207

Rigidity analysis

Rigidity analysis was performed with the CNA software package (34). CNA efficiently decomposes a constraint network into rigid clusters and connecting flexible hinge regions applying rigidity theory (56). The inherent long-range aspect to rigidity percolation (*i.e.*, whether a region is flexible or rigid) can depend on structural details that are far away, making rigidity analysis an attractive tool for studying altered structural stability due to distant influences (57, 58). Networks of covalent and noncovalent (hydrogen bonds including salt bridges and hydrophobic tethers) interactions were constructed with the Floppy Inclusions and Rigid Substructure Topography software (v.6.2) (59), to which CNA is a front- and back-end, from conformational ensembles extracted from MD trajectories of the p.A71E variant of TAUT of 1 μs length. The strengths of hydrogen bonds (including salt bridges) were assigned by the energy E_{HB} computed by the Floppy Inclusions and Rigid Substructure Topography software (60). Hydrophobic interactions between carbon or sulfur atoms were taken into account if the distance between these atoms was less than the sum of their van der Waals radii (C: 1.7 Å; S: 1.8 Å) plus an offset of $D_{cut} = 0.25$ Å (61). In order to elucidate the hierarchy of structural stability in a biomolecule (62), a constraint dilution trajectory of network states {σ} was analyzed, which was generated by successively removing hydrogen bond constraints (including salt bridges) in the order of increasing strength (61–64). Thus, only those hydrogen bonds are retained in a network of state σ that have an energy $E_{HB} \leq E_{cut}$ (σ). Altered biomolecular stability along a constraint dilution trajectory was quantified based on neighbor stability maps ($rc_{ij,\ neighbor}$ with i, j being residue numbers; Eq. 1) (65).

$$rc_{ij} = \min\{E_{cut} | \exists c \in C^{E_{cut}} : R_i \Lambda R_j \in c\} \quad (1)$$

Here, only short-range rigid contacts were considered that have ≥1 pair of heavy atoms of the residue pair $R_{\{i,j\}}$ separated by a distance ≤4.5 Å (66). A rigid contact rc_{ij} between pairs of residues ceases to exist when both residues stop sharing the same rigid cluster c of a set of rigid clusters $C^{E_{cut}}$. The double sum (Eq. 2)

$$E_{CNA} = \sum_i^n \sum_{j>i}^n rc_{ij,neighbor} \quad (2)$$

yields the chemical potential energy (E_{CNA}) due to noncovalent bonding, obtained from the coarse-grained, residue-wise network representation of the underlying biomolecular structure (35, 65). A per-residue decomposition of Eq. 2 yields the chemical potential energy of residue i because of the n short-range rigid contacts the residue is involved in (Eq. 3):

$$E_{i,CNA} = \frac{1}{2} \sum_{j \neq i}^n rc_{ij,neighbor} \quad (3)$$

For evaluating differences between wild-type TAUT and the p.A78E variant, the side chain of E78 in conformations of the

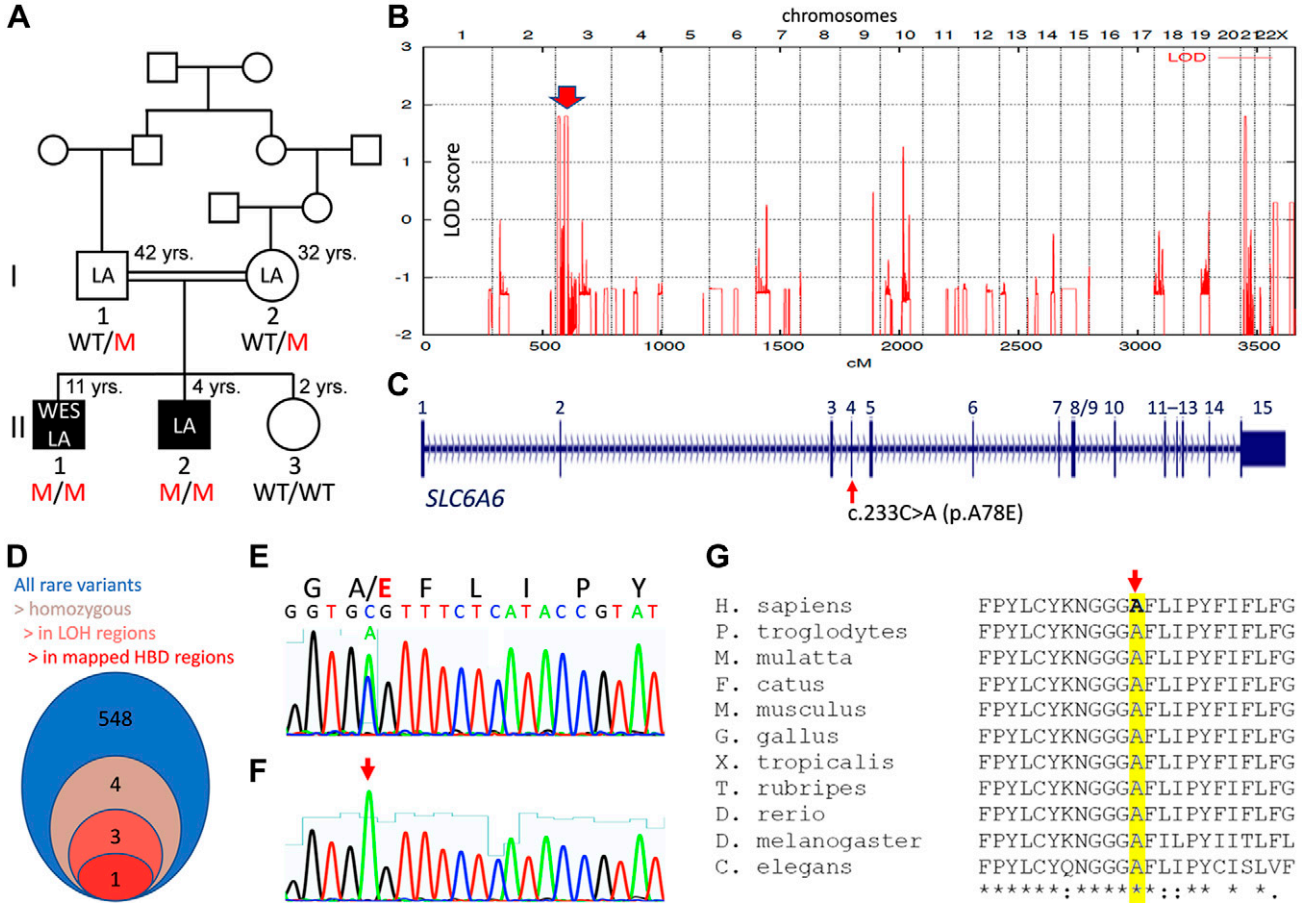

Figure 3. Genetic findings. *A*) The patients' parents are first cousins once removed. *B*) Linkage analysis using a 25-k marker panel equally spaced by 100 kb identified 3 HBD regions on chromosomes 3 and 21. *C*) Scheme of the *SLC6A6* gene with the c.233C>A (p.A78E) mutation in exon 4. *D*) Progressive filtering of WES data in patient II:1. *E*) Electropherogram from Sanger sequencing of a heterozygous carrier (parent). *F*) Electropherogram of patient II:1: homozygous *SLC6A6* mutation. *G*) The p.A78E mutation affects an evolutionarily highly conserved TAUT residue (*Homo sapiens, Pan troglodytes, Macaca mulatta, Felis catus, Mus musculus, Gallus gallus, Xenopus tropicalis, Takifugu rubripes, Danio rerio, Drosophila melanogaster, Caenorhabditis elegans*). LA, linkage analysis; LOH, loss of heterozygosity; M, *SLC6A6* mutation; WT, wild type.

TABLE 8. *Rare variants identified in WES of the index patient, II:1, and diseases known to be associated with the respective genes*

Gene	Chr	Transcript	DNA variant	Protein variant	Function, known disease	MAF (%); rs number	homo/ hemi (gnomAD)	Patho-genic	HBD region	Mapped HBD or cosegregation
SLC6A6	3	NM_003043.5	c.233C>A	p.(Ala78Glu)	Taurine transport	-	—	8/9	Yes	Yes
FAT3	11	NM_001008781.2	c.5671A>G	p.(Ile1891Val)	Cell adhesion, CNS development	0.05, rs573703666	—	0/8	Yes	No
SLC12A2	5	NM_001046.2	c.602_604del	p.(Asp202del)	Hearing, Kilquist syndrome	—	—	—	Yes	No
FAM162B	6	NM_001085480.3	c.400C>T	p.(Arg134*)	Membrane component	0.015, rs201342470	2	3/3	No	No
MID1	X	NM_000381.3	c.724G>T	p.(Ala242Ser)	Ubiquitin ligase, Opitz syndrome	0.0005, —	—	4/10	NA	NA

A hemizygous X-chromosomal variant in *MID1* is also displayed because it resides in a region for which both brothers have identical haplotypes (SNP-based genome-wide linkage analysis). The phenotype of the patients does not correspond to the syndromes resulting from pathogenic hemizygous *MID1* or homozygous *SLC12A2* variants, respectively. Chr, chromosome; *FAM162B*, family with sequence similarity 162 member B; *FAT3*, FAT atypical cadherin 3; gnomAD, Genome Aggregation Database; homo/hemi, homo- or hemizygous; *MID1*, (midline 1); NA, not applicable; rs, Reference SNP cluster ID.

p.A78E variant (ground state) was removed except for the C_β atom, leaving all other atom coordinates unchanged (yielding the "perturbed state"). In order to detect altered stability characteristics due to the mutation, a linear response approximation was then applied to obtain a per-residue decomposition of the free energy associated with the change in biomolecular stability due to the mutated residue (Eq. 4)

$$\Delta G_{i,\mathrm{CNA}} = \alpha\left(\left\langle E_{i,\mathrm{CNA}}^{\mathrm{perturbed}}\right\rangle - \left\langle E_{i,\mathrm{CNA}}^{\mathrm{ground}}\right\rangle\right) \quad (4)$$

RESULTS

Ophthalmologic characterization of 2 brothers with panretinal degeneration

The index patient (II:1, 11 yr old) was first referred for ophthalmologic examination at the age of 1.25 yr because of pendular nystagmus from birth. BCVA of 1.0 logMAR could first be determined at 23 mo of age using TACs. In the longitudinal examination, BCVA improved to 0.8 logMAR (tested with Landolt rings) and remained there up to the last examination at 11.25 yr of age. The younger brother (II:2, 4 yr old) had congenital nystagmus and was first presented for ophthalmologic examination at 6 mo of age. BCVA of 2.0 logMAR was determined at the age of 1.5 yr with TACs. Testing at the age of 3.4 yr revealed an improvement to 1.15 logMAR that remained stable until the age of 4.5 yr (Lea test). Both patients were severely hyperopic (**Fig. 1*A*, *B***).

Color vision testing in II:1 indicated a more pronounced blue color vision reduction (Fig. 1*C* and **Table 1**).

GVF testing in follow-up was only possible in the elder patient and with binocular testing of target V/4e. At last follow-up, the visual field in patient II:1 was severely reduced to 10–15° in both eyes with target V/4e and to 3° with target III/4e of GVF. Within 5 yr of visual field testing, ~75% of the visual field was lost, with 12% of normal visual field remaining (Fig. 1*D*). Patient II:2 was unable to complete GVF testing at the age of 4 yr. Finger perimetry estimated a binocular horizontal visual field of 40° and a vertical visual field of 20–25° at 3.6 yr of age. GVF and BCVA reflected severe functional impairment and were accompanied by responses below threshold in ffERG and uncorrelated responses in mfERG in patient II:1 at the age of 6.25 yr (unpublished results).

Funduscopy was limited by nystagmus and limited cooperation. No fine structural changes were visualized, and no obvious changes were seen. Fundus photography in patient II:1 at the age of 10.7 yr revealed gray-whitish spots, areas of hypo- and hyperpigmentation in the periphery, and some glistening in the macular area compatible with microglia pathology. Wide-field fundus photography showed a spotty appearance and attenuated vessels in both patients (**Fig. 2*A***).

Spectral domain OCT recordings showed a general reduction of the entire retinal thickness at all ages (Fig. 2*B–G*) compared with an age-similar healthy control (Fig. 2*H*), mainly resulting from a loss of photoreceptor cells [from the inner segment (IS) to the outer segment (OS) layer] but also of the outer plexiform layer and outer nuclear layer. The inner retinal layers [from ganglion cell layer (GCL) to inner nuclear layer (INL)] were thinner at a younger age. These layers became thicker over time in patient II:1 (Fig. 2*I*). The foveal scans indicated the

presence of altered outer photoreceptor layer structures (IS to OS) that did not change considerably in patient II:1 over the 5-yr follow-up period (Fig. 2*I*). At the age of 11.25 yr, patient II:1 presented with macular edema in the INL of the left eye (Fig. 2*D*) that decreased with Brinzolamid therapy over a period of 5 mo (Fig. 2*D–F*).

Hearing and olfaction

Patient II:1 showed normosmia (7/7 items identified), and patient II:2 showed hyposmia (4/7 items identified). Both patients had normal inner ear function in the pure tone audiogram and in the distortion product otoacoustic emissions.

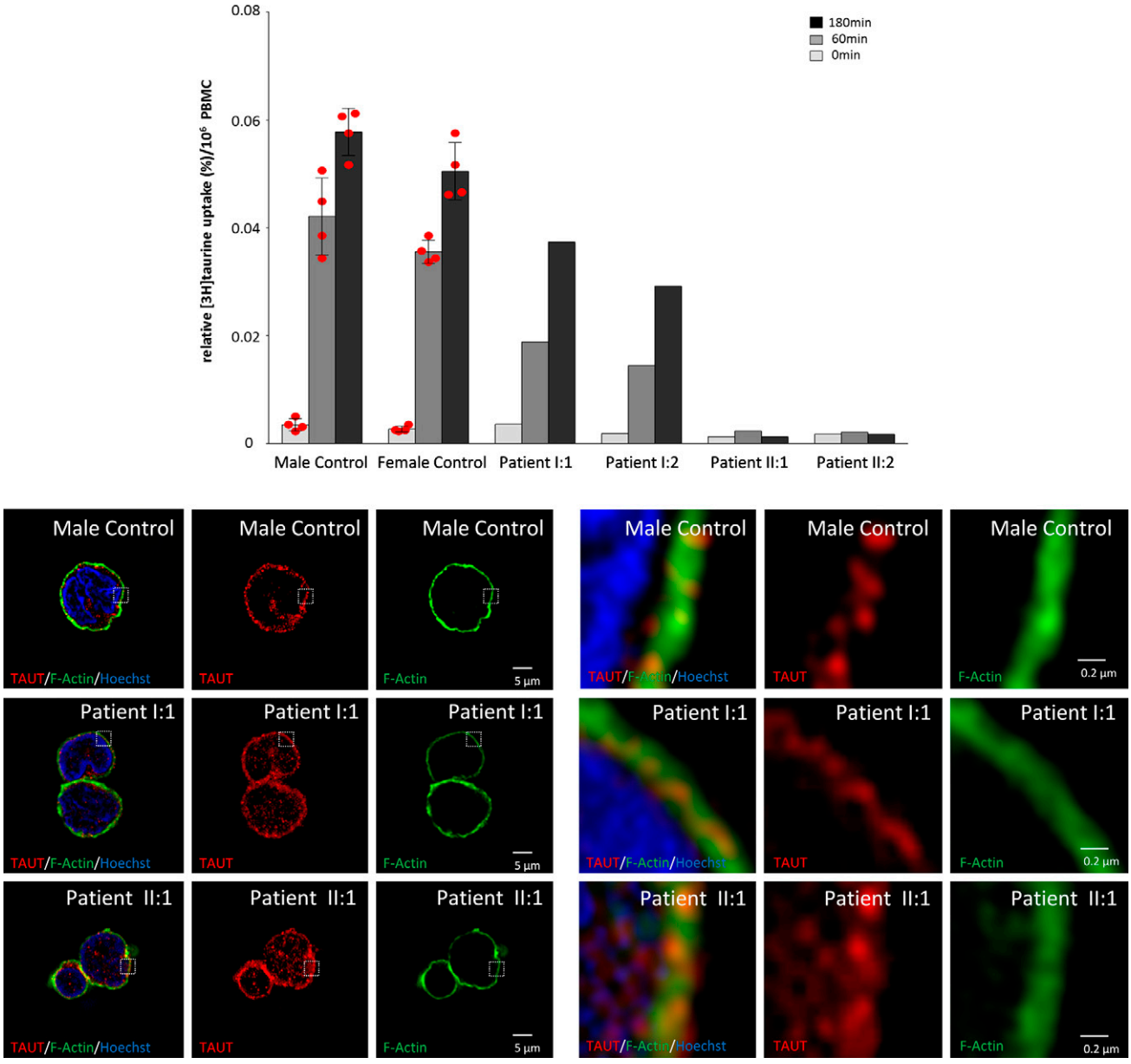

Figure 4. Taurine uptake and TAUT expression in human PBMCs. PBMCs were isolated from the peripheral blood of 4 healthy adult males (control) and 4 healthy adult females (control), the heterozygous parents, and the homozygous children (4 and 11 yr old). Upper panel: taurine uptake into human PBMCs. Cell suspensions were incubated for 0, 60, and 180 min with [^{3}H] taurine [10 µM taurine and 5.6 nM [^{3}H] taurine (0.1µCi/ml)]. The [^{3}H] taurine content was measured in the supernatants and PBMC lysates by scintillation counting, respectively. The taurine uptake by PBMCs is expressed as the percentage of total [^{3}H] taurine (added to the cell suspension) normalized to the number of cells incubated. Data are given as the mean ± SEM from 4 male and 4 female controls, and the individual values are shown separately as dots. Lower panel: TAUT expression in human PBMCs from a male (40 yr old) healthy control, the heterozygous father, and patient II:1. PBMCs were fixed, and TAUT expression was analyzed by immunofluorescence and SR-SIM. TAUT is stained in red, filamentous actin (F-Actin) is stained in green using phalloidin-FITC, and nuclei are counterstained in blue using Hoechst 34580. Boxed inserts were electronically magnified and shown on the right side.

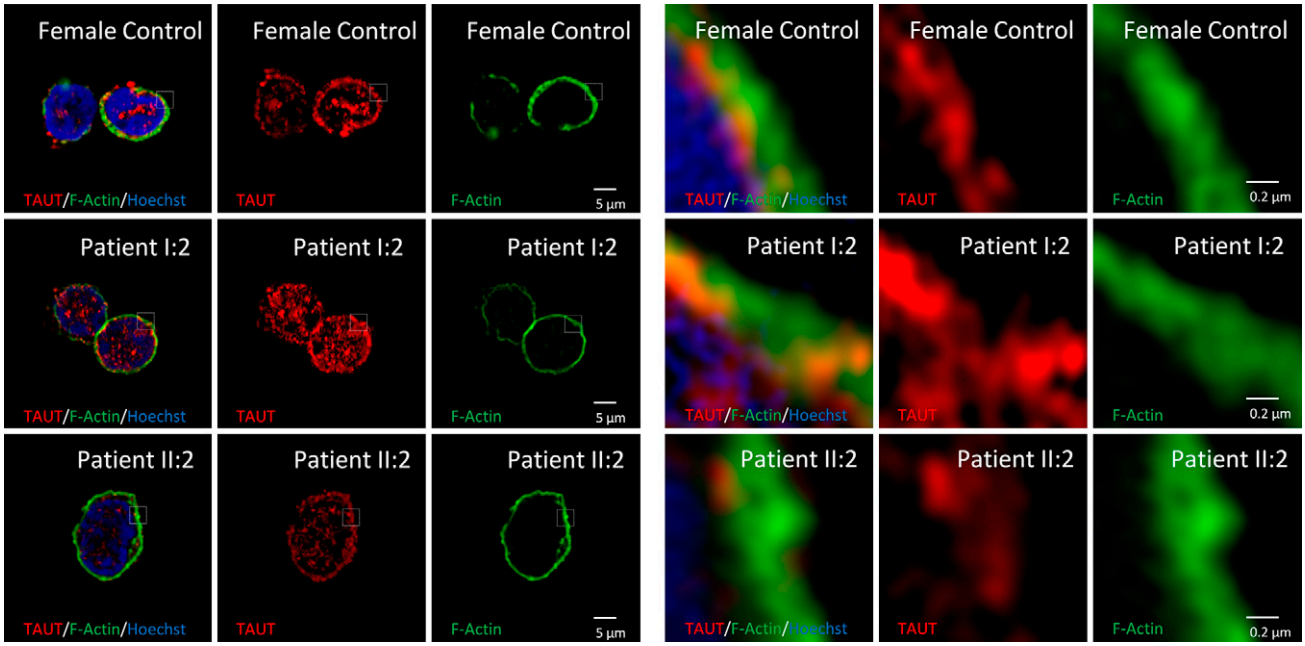

Figure 5. TAUT expression in human PBMCs. PBMCs were isolated from a female (38 yr old) healthy control, the mother (heterozygous carrier), and patient II:2 (homozygous mutation). PBMCs were fixed, and TAUT expression was analyzed by immunofluorescence and SR-SIM. TAUT is stained in red, filamentous actin (F-Actin) is stained in green using phalloidin-FITC, and nuclei are counterstained in blue using Hoechst 34580. Boxed inserts were electronically magnified and shown on the right side.

General clinical assessment and indication for increased RNA oxidation and ongoing oxidative stress

Patient II:1 (body mass 45 kg, height 146 cm) and patient II:2 (body mass 18 kg, height 106 cm) underwent clinical examination. Both showed no obvious cognitive deficiencies except those related to visual impairment. Physical examination and abdominal sonography revealed no abnormalities. Transient elastography (FibroScan) and CAP testing gave no evidence for liver fibrosis or steatosis (**Table 2**). Electrocardiograms were normal in both patients. C-reactive protein, creatine kinase, lactate dehydrogenase, aspartate aminotransferase, alanine aminotransferase, γ-glutamyl transferase, bilirubin, and alkaline phosphatase in the serum were normal. Hemoglobin was slightly elevated, and the eosinophil count was 1730/µl in patient II:1 but normal in patient II:2. Serum concentrations of bile acids were normal, and despite strongly lowered serum taurine levels to 4 µM in both patients (**Table 3**), the concentrations of taurine- and glycine-conjugated bile acids were normal (**Tables 4** and **5**). Except for taurine, the concentrations of other amino acids in the plasma were normal (**Tables 6** and **7**). Taurine excretion into the urine was normal (patient II:1) or even somewhat elevated (patient II:2) in the patients, whereas serum taurine levels and urinary excretion of taurine were in the normal range in the noncarrier daughter and in the heterozygous parents (Table 3). Both patients exhibited strongly increased urinary excretion of 8-oxo-Gsn, suggestive of increased RNA oxidation and ongoing oxidative stress. An increased 8-oxo-Gsn excretion into urine, albeit to a lesser extent, was observed in the heterozygous parents, whereas the noncarrier daughter showed normal values (Table 3).

Homozygous *SLC6A6* mutation underlies taurine deficiency and retinal degeneration

The patients, 2 brothers originating from Turkey, have a healthy younger sister and consanguineous parents (first cousins once removed) (**Fig. 3*A***). No pathogenic variant was identified in patient II:1 by targeted NGS of 138 retinal degeneration genes. Linkage analysis of genotyping data using a reduced panel of 25,000 markers (25k), equally

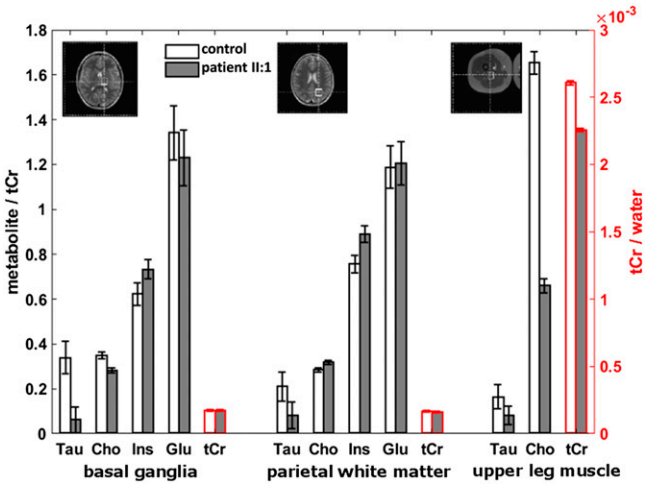

Figure 6. Metabolite:total creatine and total creatine:water ratios in basal ganglia, parietal white matter, and upper leg muscle of a healthy control and patient II:1. Note that taurine:total creatine ratios were reduced in the patient, whereas total creatine:water ratios did not differ between patient and control. Cho, choline; Glu, glutamate; Ins, Inositol; Tau, taurine; tCr, total creatine. Error bars indicate CRLB. Black-lined columns relate to left *y* axis, and red-lined columns relate to right *y* axis.

TABLE 9. *Metabolite:total creatine and total creatine:water ratios in basal ganglia, parietal white matter, and upper leg muscle of a healthy control and patient II:1*

	CRLB (%)					
	Basal ganglia		Parietal white matter		Upper leg muscle	
Ratio	Control	Patient	Control	Patient	Control	Patient
Taurine:tCr	0.340 (22)	0.06 (95)	0.210 (31)	0.08 (73)	0.163 (33)	0.08 (51)
Inositol:tCr	0.626 (8)	0.736 (6)	0.759 (5)	0.891 (4)	—	—
Choline:tCr	0.352 (4)	0.282 (4)	0.283 (3)	0.321 (3)	1.656 (3)	0.662 (5)
Glutamate:tCr	1.344 (9)	1.231 (10)	1.189 (8)	1.206 (8)	—	—
tCr:water	1.72E−04 (3)	1.70E−04 (3)	1.64E−04 (3)	1.57E−04 (3)	2.61E−03 (6)	2.26E−03 (5)

Note that taurine:total creatine ratios were reduced in the patient, whereas total creatine:water ratios did not differ between patient and control. tCr, total creatine.

spaced by 100 kb and with a MAF of 0.15, revealed regions of homozygosity by descent (HBD) on chromosomes 3p26.3-p26.1 (3.227 Mb), 3p25.1-p24.1 (14.243 Mb), and 21q21.1-q21.3 (5.418 Mb). In all 3 regions, the calculated LOD score reached the theoretical maximum LOD score of 1.8 estimated beforehand for this family (Fig. 3*B*). Using 100,000 or all applicable markers of the array resulted in some additional small HBD regions reaching a maximum LOD score of 1.8 (results not published because none of the homozygous SNVs of the patient were contained in any of these regions). WES generated 10 Gb of sequence, and 79% of the target sequence covered more than 30×. Among 548 rare variants, 4 were homozygous. Further filtering with homozygosity stretches (loss of heterozygosity regions) identified by successive homozygous SNVs across genes resulted in 3 homozygous variants. The only homozygous variant localized in a mapped HBD region was NM_003043.5:c.233C>A in *SLC6A6* (chromosome 3p25.1), replacing the evolutionarily highly conserved residue NP_003034.2:p.A78E (Fig. 3*B–D*, *F–G*, **Table 8**). Segregation analysis confirmed homozygosity of the *SLC6A6* mutation in both patients, and the parents were heterozygous carriers (Fig. 3*C–G*). The healthy sister was homozygous for the wild-type allele.

Studies on taurine transport

Both patients (II:1 and II:2) had low (4 μM) serum taurine levels but normal taurine excretion into the urine, which is probably due to impaired reabsorption in the kidney (Table 3). Taurine transport was studied in PBMCs, which

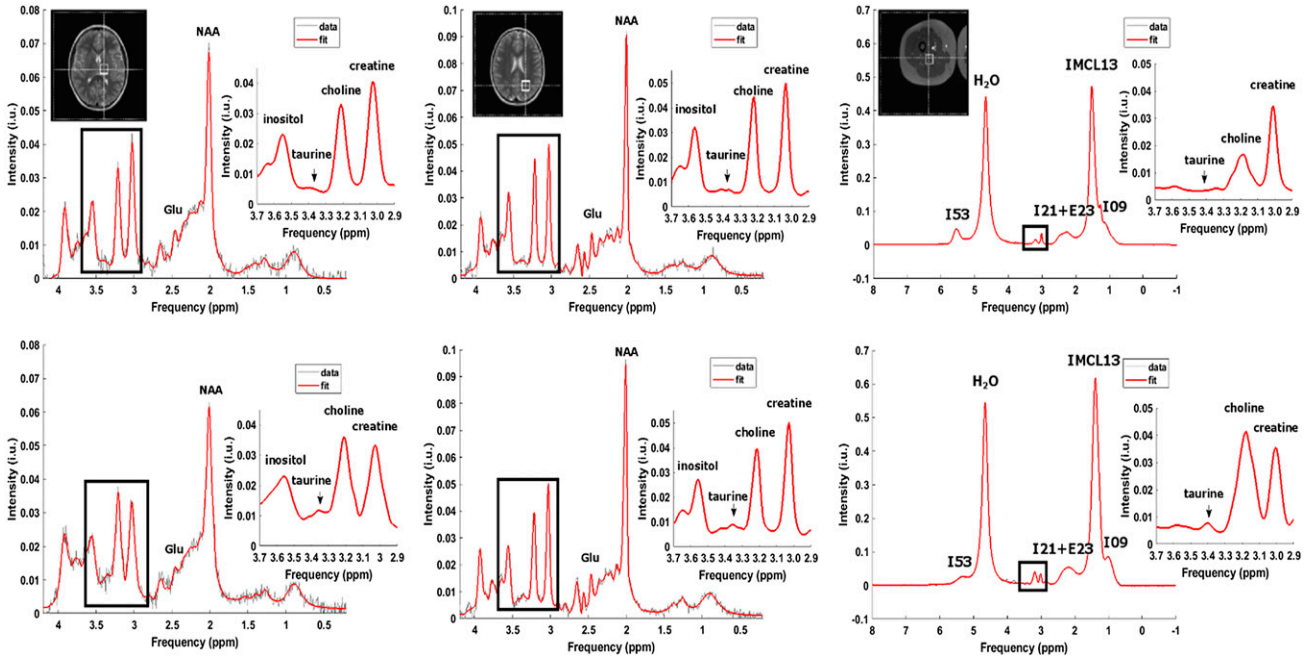

Figure 7. MRS of patient II:1 (top row) and a healthy control (bottom row). The spectra of basal ganglia (first column), parietal white matter (second column), and upper leg muscle (third column) are normalized to the unsuppressed water reference and reported in institutional units (i.u.). Gray curves represent the MRS data, and red curves represent the LCModel fit. The voxel localization is depicted for the patient's measurement. The taurine peak shows up at ~3.4 ppm (see magnified insert). Further prominent peaks are labeled. E, extramyocellular lipid; Glu, glutamate; NAA, *N*-acetyl-aspartate; I, intramyocellular lipid; IMCL13, intramyocellular lipid 13.

express TAUT. [^{3}H] taurine uptake by PBMCs was decreased by ~95% in patients II:1 and II:2 (**Fig. 4**). When [^{3}H] taurine uptake into PBMCs within 60 min is taken as a rough estimate for the initial rate of taurine uptake, the uptake rates in the heterozygous parents were only about one-half of the transport found in healthy sex-matched controls, suggestive of a gene dosage effect (Fig. 4). Immunocytochemistry showed that the defective TAUT still localized in the plasma membranes of PBMCs (Figs. 4 and **5**), indicating that the TAUT mutation did not significantly interfere with TAUT targeting to the plasma membrane. As shown by proton MRS, the homozygous TAUT mutation led to low taurine levels in the brain and in skeletal muscle (**Fig. 6** and **Table 9**). **Figure 7** depicts the quantified magnetic resonance spectra, including MRS data and the estimated LCModel fit as well as the voxel localization. Only patient II:1 was examined. The patient's spectra are characterized by the absence of a taurine peak at 3.4 ppm (Fig. 7 top row). The estimated

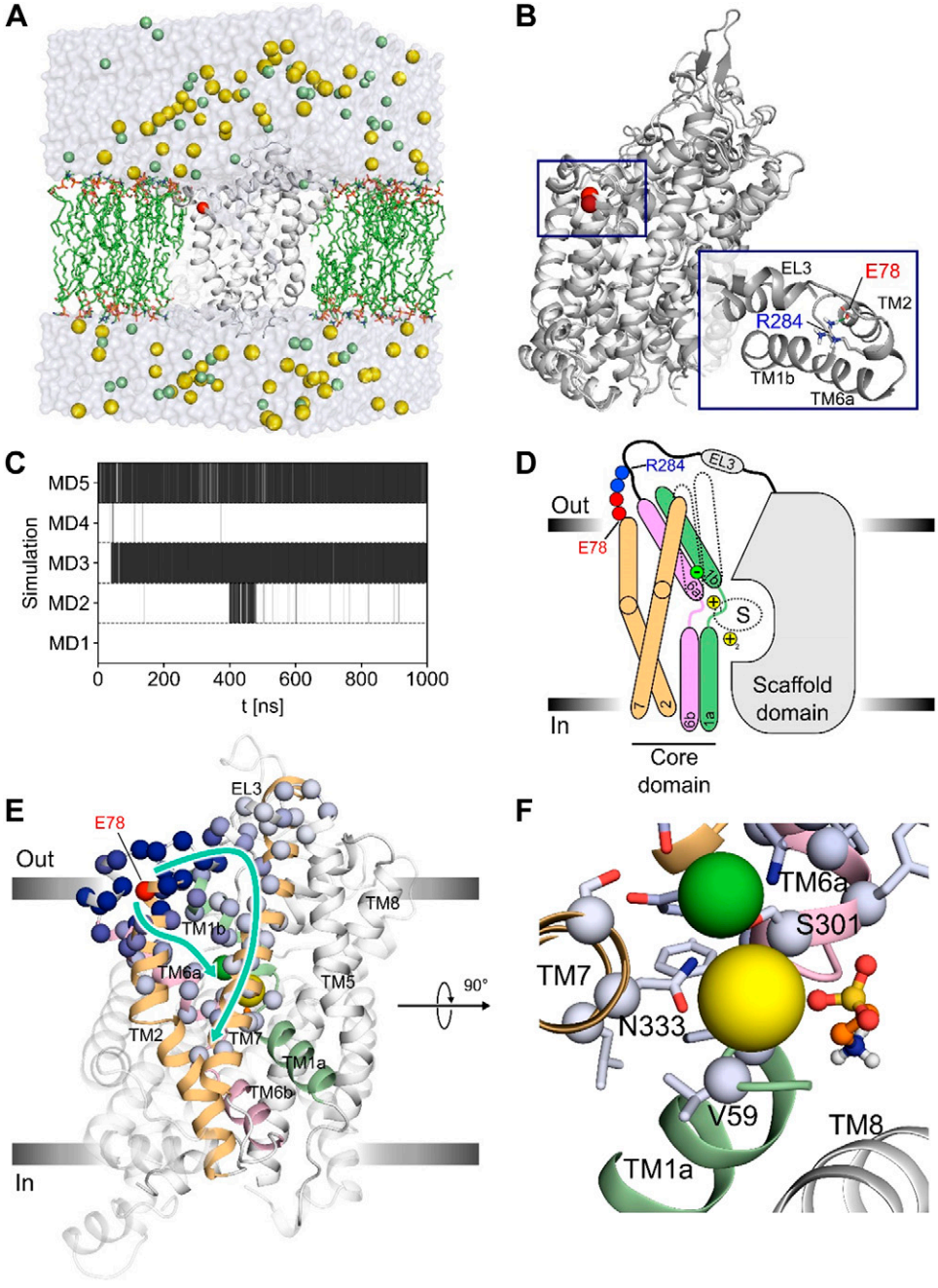

Figure 8. Structural analysis of the impact of the p.A78E mutation. *A*) Illustration of the simulated TAUT system. TAUT is depicted in white cartoon representation, membrane lipids are depicted as green sticks, sodium and chloride ions are depicted as yellow and green spheres, respectively, and water molecules are shown in a light-blue surface representation. The location of residue 78 is highlighted with a red sphere. *B*) Overlay of the closest-to-the-mean structures obtained from the MD simulations of wild-type TAUT (white) and its p.A78E variant (gray). The location of residue 78 is highlighted with a red sphere. The inset shows the salt bridge formed between residues p.E78 and p.R284 in the p.A78E variant. *C*) Formation of a salt bridge between p.E78 and p.R284 in the p.A78E variant. Each occurrence of a salt bridge during the 5 MD simulations is indicated by a vertical line. A salt bridge is considered present when the distance between the donor atom and the acceptor atom is less than 3.0 Å and the angle (donor atom, hydrogen atom, acceptor atom) is more than 135°. *D*) Schematic representation of transmembrane helix TM1a/b, TM2, TM6a/b, and TM7 that undergoes substantial changes in positions during a transport cycle, as indicated by TM1b/6a movements upon going from a substrate-free to a substrate-bound state and hinges (circles) in TM2/7. The salt bridge between p.E78 and p.R284 is indicated. +, Na^+-1 and Na^+-2 binding site; −, Cl^- binding site; S, substrate binding site. *E*) Spheres represent residues whose structural stability is markedly increased in the p.A78E variant compared with the wild type; blue colors indicate predicted $\Delta G_{i,CNA}$ (see rigidity analysis Eq. 4 in Materials and Methods; Fig. 11), with darker colors indicating larger values. Residue 78 is shown in red. The 2 arrows indicate 2 potential routes through which altered structural stability is propagated to residues lining the potential taurine (sticks-and-balls representation), Na^+-1 (yellow sphere), and Cl^- (green sphere) binding sites. TMs 1b, 6a, and 2/7 are colored green, pink, and orange, respectively. Gray bars indicate the location of the lipid head groups in the upper and lower membrane leaflet. *F*) Blow-up of the potential taurine, Na^+-1, and Cl^- binding sites, residues of which are affected by the change in structural stability. See previous description (*E*) regarding colors.

taurine to creatine ratios and the Cramér-Rao lower bound (CRLB) as rate of the measurement error are summarized in Fig. 6 and Table 9. The taurine concentration is strongly reduced in the patient. The other quantified metabolites remained unchanged except for a strong reduction in the choline levels within the upper leg muscles of the patient.

The p.A78E mutation results in a structural stabilization of transmembrane helices 1b, 2, 6a, and 7

To assess the consequences of the mutation in TAUT at an atomistic level, MD simulations of wild-type TAUT and its p.A78E variant in an explicit solvent/explicit membrane environment were performed (**Fig. 8*A***) and subsequently analyzed (Fig. 8*B–F*). Because no experimental structural information for TAUT is available, structural models obtained by comparative modeling were used as starting structures for the wild-type and p.A78E variant simulations. The mutation did not result in pronounced global structural changes of TAUT on MD time scales of 1 μs, as depicted by the overlay of closest-to-the-mean structures (Fig. 8*B*) and quantified by RMSDs of C_α atom positions. The RMSD values between TAUT conformations of either the wild-type system or the p.A78E variant are similar to those between TAUT conformations of the wild-type system *vs.* the p.A78E variant (**Fig. 9*A, B***). This finding is irrespective of whether the highly flexible extracellular loop EL2 was considered (Fig. 9*A*) or not (Fig. 9*B*). Except for 2 residues, no changes in the residue-wise helical content were found (Fig. 9*C*), indicating the absence of local structural changes in the backbone. No pronounced difference in the membrane structure was found between the wild-type system and the p.A78E variant (**Fig. 10**), indicating unchanged interactions between the p.A78E variant and the membrane compared with the wild type.

Visual inspection of the MD trajectories revealed that the side chain of p.E78 at the N terminus of transmembrane helix (TM)2 partially forms a salt bridge interaction with p.R284 in the extracellular loop (EL)3 (Fig. 8*B*); the side chain of p.A78 cannot form such a salt bridge. Over all variant trajectories, the salt bridge is present in 40 ± 23% of the conformations (Fig. 8C), and once it is formed, it can persist for the remainder of the simulation time. The salt bridge formation links the 2 topologically distant regions EL3 and TM2 in the protein (Fig. 8*B, D*), which led us to hypothesize that this interaction increases the structural stability in certain regions of TAUT. To validate this hypothesis, we applied a rigidity theory–based perturbation approach (34, 35), which models a protein as a network of bond constraints and allows for detecting long-range stability changes due to altered bond characteristics. Approximately 25% of the TAUT residues show an increased structural stability ($\Delta G_{i,\mathrm{CNA}} \geq 0.2$ kcal/mol; Pfleger *et al.* (35); **Fig. 11**) in the p.A78E variant compared with the wild type. TAUT regions affected contain residue p.L267-P288 in the EL3 and residues p.G77-F86, p.Q289-Y302, and p.C326-F350 in the transmembrane part (Fig. 11). Notably, the p.A78E mutation

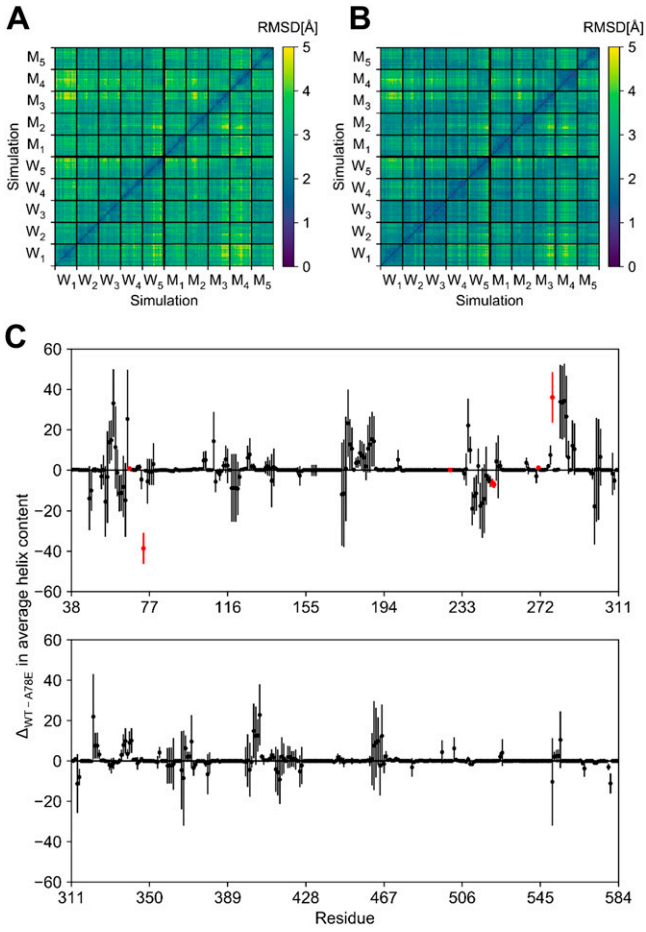

Figure 9. Structural changes of wild-type TAUT *vs.* the p.A78E variant. *A*) RMSD of the positions of all C_α atoms between the snapshots of all MD simulations. $M_{1–5}$: MD simulations of the p.A78E variant; $W_{1–5}$: MD simulations of the wild type. *B*) Corresponding data excluding the C_α atoms of residues 152–192 from the calculation. *C*) Comparison of the residue-wise helical content between wild-type and p.A78E variants. The difference was computed from means of the helical content over the respective 5 MD simulations; error bars denote SEM. Positive values indicate a higher helical content in the wild type. Statistically significant differences ($P < 0.05$) are highlighted in red.

influences residues as far as ~25 Å away from the mutation site (p.C326 in TM7 and p.F95 in TM2). Affected residues are not dispersed but reveal 2 distinct paths of how altered structural stability propagates from the mutation site through TM1b/TM6a and TM2/TM7 to the potential taurine, Na^+-1, and Cl^- binding sites in the center of TAUT (Fig. 8*E, F*).

DISCUSSION

This is the first report on human TAUT deficiency with a homozygous point mutation in the TAUT-encoding *SLC6A6* gene causing early panretinal degeneration in a consanguineous family (Fig. 3). Thinning of the retina and a severe reduction of light-induced responses in electrophysiology correspond to the findings in *Slc6a6*$^{-/-}$ mice. Both patients display early and progressive loss of rod and

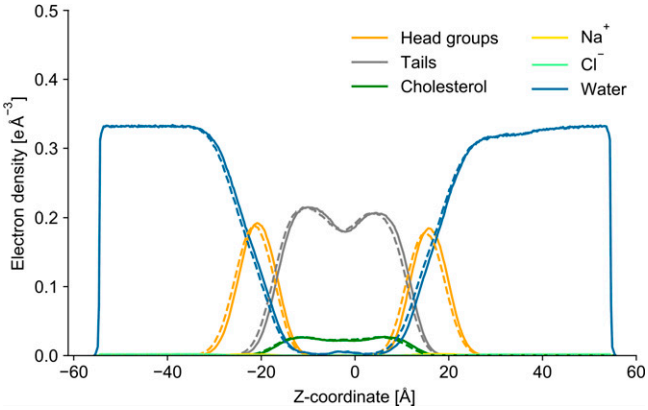

Figure 10. Distribution of system components in the MD simulations. Component density in the wild-type TAUT system (solid lines) and the p.A78E variant (dashed lines) is expressed as mean electron density of 5 MD simulations each.

cone photoreceptor cells. Residual photoreceptors in the fovea show major disorganization, resembling severe morphologic changes of photoreceptors in taurine-depleted rhesus monkeys (67, 68). Tritanopia and a general functional deficit in cone function are compatible with pronounced S-cone photoreceptor loss that has been reported together with L/M cone loss in taurine-depleted albino rats (10). Increased inner retinal thickness in our patients (Fig. 2*I*) may result from the swelling of retinal ganglion cells preceeding their primary degeneration (69).

The *SLC6A6* mutation reported herein results in an alanine to glutamate residue exchange at position 78 (p.A78E) of TAUT. Its localization in the by far largest of the mapped HBD regions is in line with the observation that homozygous pathogenic variants in patients from consanguineous families tend to reside in (one of) the largest HBD intervals (70). The mutation has apparently no or little effect on TAUT membrane localization but severely impairs taurine transport. MD simulations support localization of the p.A78E variant to the plasma membrane in that structural changes between wild-type TAUT and the p.A78E variant were not observed (Figs. 8*B* and 9*A–C*) and the membrane structure remained very similar to the wild type (Fig. 10).

As to a potential mechanism for how p.A78E interferes with taurine transport, a salt bridge between p.E78 and p.R284 was observed (Fig. 8*C*), likely favored by relocation of the p.E78 side chain to a polar protein region (Fig. 8*B*). This interaction bridges the 2 topologically distant regions EL3 and TM2, which otherwise do not interact (Figs. 8*D* and **12*A***). Furthermore, TM2 packs against TM6a/b, which, together with TM1a/b, forms the taurine, Na^+-1, and Cl^- binding sites, as inferred from an overlay of substrate-bound $LeuT_{Aa}$ structures (Fig. 12*B*) (39, 71). These findings suggested that the salt bridge interaction rigidifies functionally relevant regions of TAUT. This suggestion was verified by a rigidity theory–based perturbation approach (57, 58): the results reveal that an increase in structural stability percolates from the site of salt bridge formation in TM2 *via* 2 paths toward the binding sites of taurine, Na^+-1, and Cl^- (Fig. 8*E*, *F*). The involved transmembrane helices undergo substantial positional changes during a transport cycle (30) (Fig. 8*D*). Taken together, our results suggest that the structural stabilization of these critical elements either hampers binding of the cargo by fostering binding-incompetent TAUT conformations or prevents conformational changes required for the transport cycle (30).

In line with the MD simulations, taurine uptake into PBMCs was decreased by ~95%, and proton MRS showed severe taurine depletion of both skeletal muscle and brain. Normal taurine excretion into the urine despite very low taurine concentrations in serum indicated severe taurine loss in the urine caused by impaired tubular reabsorption in the kidney.

Taurine acts as an organic osmolyte, exhibits antioxidative and cytoprotective effects, is a conjugation partner (*e.g.*, for bile acids) (2–4), and may ameliorate and stabilize immunologic functions. Besides retinal degeneration within 4 wk (7, 72), multiple additional phenotypic alterations have been identified in TAUT-knockout mice (4): skeletal and cardiac muscle abnormalities at later age (5), liver fibrosis (6), hearing loss, altered synaptic plasticity and behavior, and increased mortality with regard to plasmodium infections due to overwhelming cytokine release. Although the patients in our study displayed retinal degeneration without other detectable organ manifestations, significantly increased urinary excretion of 8-oxo-Gsn indicated generally enhanced oxidative stress and RNA oxidation. It is currently not clear whether a "taurine deficiency syndrome" comparable with the multisystemic abnormalities in the mouse model will manifest in the patients at an older age. Therefore, continuous surveillance is warranted to detect additional symptoms as early as possible.

More than 200 genes are known to be implicated in retinal degeneration (73). Except retinal pigment epithelium 65 (*RPE65*) gene therapy (74), no causative treatments are available to date. Unspecific therapeutic

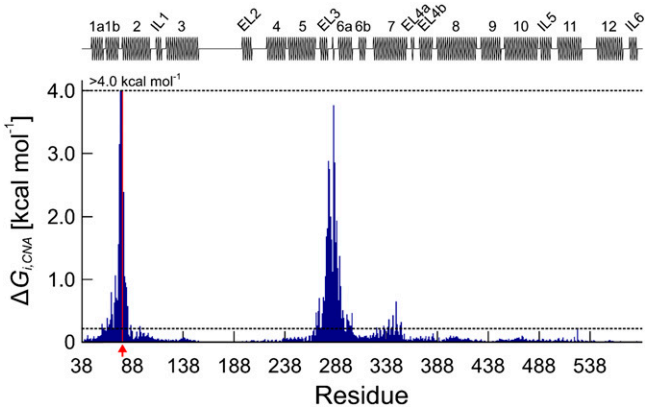

Figure 11. Per-residue free energy associated with the change in biomolecular stability due to the p.A78E mutation (Eq. 4). Secondary structure information of TAUT is shown at the top. The red bar and arrow denote the mutation site. The dashed line at 0.2 kcal/mol indicates the threshold above which residues are considered perturbed (47). EL, extracellular loop; IL, intracellular loop.

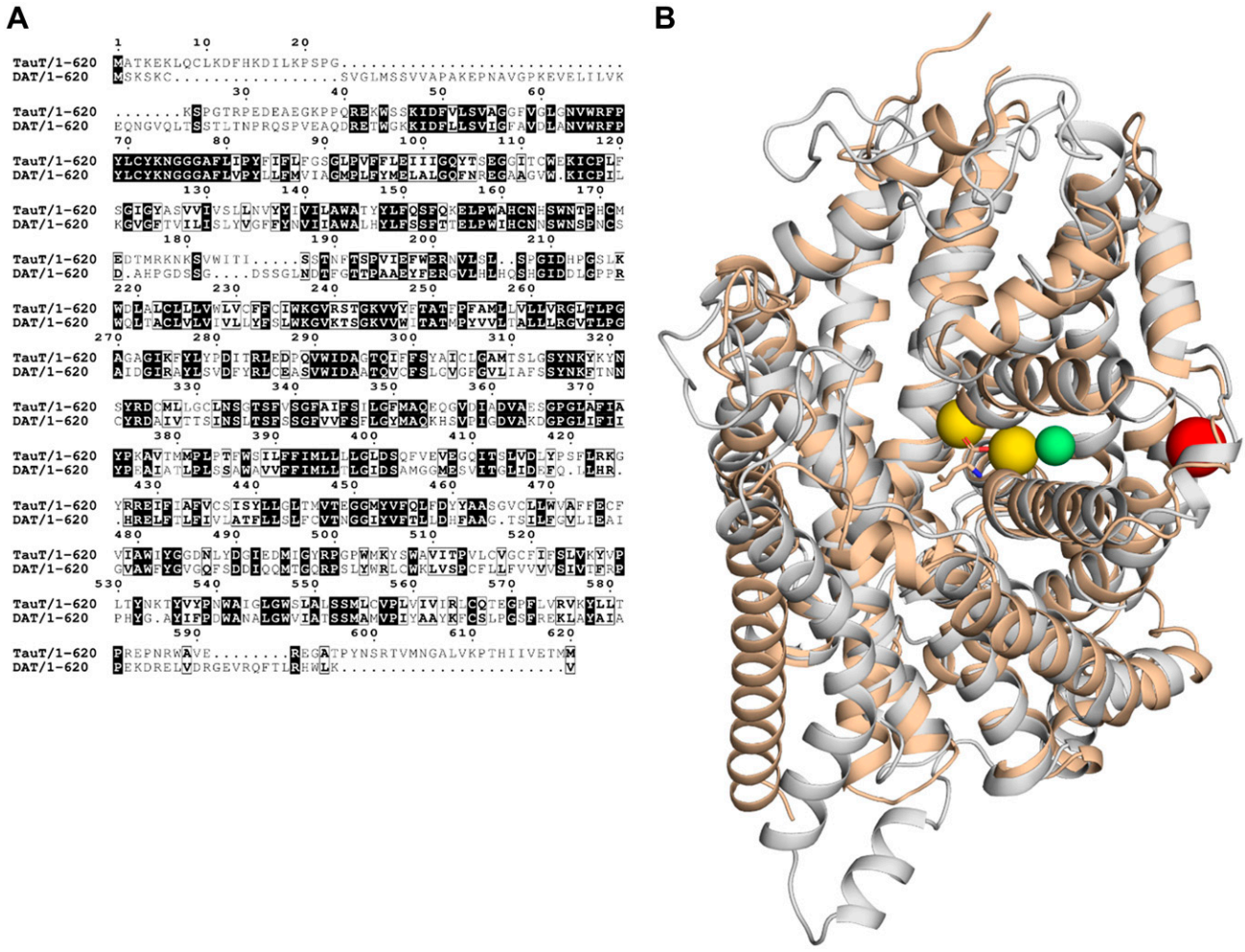

Figure 12. Sequence alignment and structural overlay with respect to TAUT. *A*) Sequence alignment of human TAUT and DAT. *B*) Overlay of the TAUT wild-type structure (white) and the Na^+- and Cl^--bound crystal structure of $LeuT_{Aa}$ (PDB ID: 4HOD) (41). The mutation site in TAUT is highlighted with a red sphere. Sodium and chloride ions are shown as yellow and green spheres, respectively.

strategies (*e.g.*, with neuroprotective factors aimed at delaying cell death) may at the most provide a longer time window for future causal treatment (75). For some retinopathies, specific compounds for effective treatment have been identified, but this usually requires large-scale screening of substances (76, 77). Here, the situation is different: the specific "therapeutic compound" would target taurine homeostasis (provided its defective TAUT-mediated transport can be bypassed) to prevent retinal degeneration and potential further organ pathologies in later life. Because simple taurine substitution is probably not effective because of impaired renal reabsorption of the amino acid, the application of taurine conjugates taken up into the cells and subsequently hydrolyzed intracellularly could represent a promising approach. Further organic osmolytes with protein stabilizing activity, such as betaine, myo-inositol, or α-glycerophosphorylcholine, have not been tested yet regarding their potency to substitute for taurine.

SLC6A6-associated retinal dystrophy is probably rare but these patients can quickly be identified by subnormal plasma taurine levels as a diagnostic biomarker; a quick and inexpensive test to identify patients eligible for *SLC6A6* mutation analysis and, hopefully soon, effective treatment. FJ

ACKNOWLEDGMENTS

The authors thank Mrs. Ursula Wiggen (University Hospital Düsseldorf–Heinrich Heine University Düsseldorf) for the patient handling during the magnetic resonance spectroscopy measurement, Dr. Ute Albrecht for coordinating clinical examinations and Ina Park for *SLC6A6* mutation analyses. The authors are grateful for computational support and infrastructure provided by the Zentrum für Informations und Medientechnologie (ZIM) at Heinrich Heine University Düsseldorf, and the computing time provided by the John von Neumann Institute for Computing (NIC) to H.G. on the supercomputer Jülich Wizard for European Leadership Science (JUWELS) at the Jülich Supercomputing Centre (JSC) (ID: HKF7). This study was supported by grants from PRO RETINA Deutschland, Stiftung Auge (Deutsche Ophthalmologische Gesellschaft), Dr. Senckenbergische Stiftung; the Deutsche Forschungsgemeinschaft (DFG; Projektnummer 190586431-SFB

974) Communication and Systems Relevance in Liver Injury and Regeneration (Düsseldorf, Germany), and Research Group FOR 2518 DynIon (Project P7, GO 1367/2-1 to H.G.). M.N.P. and B.G. are joint first authors. D.H. and H.J.B. share senior authorship. The authors declare no conflicts of interest.

AUTHOR CONTRIBUTIONS

H. J. Bolz designed and supervised study, acquired and analyzed genetic data, and wrote the manuscript; U. Zechner acquired and analyzed genetic data and wrote manuscript; B. S. Budde performed linkage analysis and wrote the manuscript; M. R. Toliat performed and analyzed genome-wide single-nucleotide polymorphism genotyping; J. Altmüller performed whole-exome sequencing and wrote the manuscript; P. Nürnberg acquired and analyzed genetic data; M. N. Preising designed and supervised study, performed patient sampling and handling, performed the compilation and presentation of ophthalmic data, and wrote the manuscript; C. Friedburg examined patients, acquired and analyzed ophthalmic and electrophysiology data; B. Lorenz provided critical review of the data and manuscript; B. Görg performed cell biological experiments, analyzed data, and wrote the manuscript. N. Qvartskhava performed transport studies; M. Beyer performed clinical examination; H. J. Zöllner performed and analyzed magnetic resonance spectroscopy (MRS); H.-J. Wittsack performed and analyzed MRS; J. Schaper performed and analyzed MRS; D. Klee performed and analyzed MRS; A. Schnitzler performed and analyzed MRS and wrote the manuscript; J. Schipper performed ear, nose, and throat examinations; M. Bonus performed and analyzed molecular dynamics simulations and contributed to writing the manuscript; C. Pfleger performed and analyzed rigidity analysis and contributed to writing the manuscript; H. Gohlke planned molecular simulations and analyzed data, and wrote the manuscript; D. Herebian analyzed amino acids, bile acids, and 8-oxo-7,8-dihydroguanosine; D. Häussinger designed and supervised study, analyzed data, and wrote the manuscript; and all authors performed a critical revision of the manuscript for important intellectual content and final approval of the manuscript.

REFERENCES

1. Liu, Q. R., López-Corcuera, B., Nelson, H., Mandiyan, S., and Nelson, N. (1992) Cloning and expression of a cDNA encoding the transporter of taurine and beta-alanine in mouse brain. *Proc. Natl. Acad. Sci. USA* **89**, 12145–12149
2. Huxtable, R. J. (1992) Physiological actions of taurine. *Physiol. Rev.* **72**, 101–163
3. Huxtable, R. J. (2000) Expanding the circle 1975-1999: sulfur biochemistry and insights on the biological functions of taurine. *Adv. Exp. Med. Biol.* **483**, 1–25
4. Warskulat, U., Heller-Stilb, B., Oermann, E., Zilles, K., Haas, H., Lang, F., and Häussinger, D. (2007) Phenotype of the taurine transporter knockout mouse. *Methods Enzymol.* **428**, 439–458
5. Warskulat, U., Flögel, U., Jacoby, C., Hartwig, H. G., Thewissen, M., Merx, M. W., Molojavyi, A., Heller-Stilb, B., Schrader, J., and Häussinger, D. (2004) Taurine transporter knockout depletes muscle taurine levels and results in severe skeletal muscle impairment but leaves cardiac function uncompromised. *FASEB J.* **18**, 577–579
6. Warskulat, U., Borsch, E., Reinehr, R., Heller-Stilb, B., Mönnighoff, I., Buchczyk, D., Donner, M., Flögel, U., Kappert, G., Soboll, S., Beer, S., Pfeffer, K., Marschall, H. U., Gabrielsen, M., Amiry-Moghaddam, M., Ottersen, O. P., Dienes, H. P., and Häussinger, D. (2006) Chronic liver disease is triggered by taurine transporter knockout in the mouse. *FASEB J.* **20**, 574–576
7. Heller-Stilb, B., van Roeyen, C., Rascher, K., Hartwig, H. G., Huth, A., Seeliger, M. W., Warskulat, U., and Häussinger, D. (2002) Disruption of the taurine transporter gene (taut) leads to retinal degeneration in mice. *FASEB J.* **16**, 231–233
8. Vinnakota, S., Qian, X., Egal, H., Sarthy, V., and Sarkar, H. K. (1997) Molecular characterization and in situ localization of a mouse retinal taurine transporter. *J. Neurochem.* **69**, 2238–2250
9. Hayes, K. C., Carey, R. E., and Schmidt, S. Y. (1975) Retinal degeneration associated with taurine deficiency in the cat. *Science* **188**, 949–951
10. García-Ayuso, D., Di Pierdomenico, J., Hadj-Said, W., Marie, M., Agudo-Barriuso, M., Vidal-Sanz, M., Picaud, S., and Villegas-Pérez, M. P. (2018) Taurine depletion causes ipRGC loss and increases light-induced photoreceptor degeneration. *Invest. Ophthalmol. Vis. Sci.* **59**, 1396–1409
11. Ament, M. E., Geggel, H. S., Heckenlively, J. R., Martin, D. A., and Kopple, J. (1986) Taurine supplementation in infants receiving long-term total parenteral nutrition. *J. Am. Coll. Nutr.* **5**, 127–135
12. Geggel, H. S., Ament, M. E., Heckenlively, J. R., Martin, D. A., and Kopple, J. D. (1985) Nutritional requirement for taurine in patients receiving long-term parenteral nutrition. *N. Engl. J. Med.* **312**, 142–146
13. Ehnes, A., Wenner, Y., Friedburg, C., Preising, M. N., Bowl, W., Sekundo, W., Zu Bexten, E. M., Stieger, K., and Lorenz, B. (2014) Optical coherence tomography (OCT) device independent intraretinal layer segmentation. *Transl. Vis. Sci. Technol.* **3**, 1
14. Hood, D. C., Bach, M., Brigell, M., Keating, D., Kondo, M., Lyons, J. S., Marmor, M. F., McCulloch, D. L., and Palmowski-Wolfe, A. M.; International Society For Clinical Electrophysiology of Vision. (2012) ISCEV standard for clinical multifocal electroretinography (mfERG) (2011 edition). *Doc. Ophthalmol.* **124**, 1–13
15. McCulloch, D. L., Marmor, M. F., Brigell, M. G., Hamilton, R., Holder, G. E., Tzekov, R., and Bach, M. (2015) ISCEV Standard for full-field clinical electroretinography (2015 update). *Doc Ophthalmol* **130**, 1–12
16. Rüschendorf, F., and Nürnberg, P. (2005) ALOHOMORA: a tool for linkage analysis using 10K SNP array data. *Bioinformatics* **21**, 2123–2125
17. Abecasis, G. R., Cherny, S. S., Cookson, W. O. C., and Cardon, L. R. (2001) GRR: graphical representation of relationship errors. *Bioinformatics* **17**, 742–743
18. O'Connell, J. R., and Weeks, D. E. (1998) PedCheck: a program for identification of genotype incompatibilities in linkage analysis. *Am. J. Hum. Genet.* **63**, 259–266
19. Abecasis, G. R., Cherny, S. S., Cookson, W. O., and Cardon, L. R. (2002) Merlin–rapid analysis of dense genetic maps using sparse gene flow trees. *Nat. Genet.* **30**, 97–101
20. Thiele, H., and Nürnberg, P. (2005) HaploPainter: a tool for drawing pedigrees with complex haplotypes. *Bioinformatics* **21**, 1730–1732
21. Kawalia, A., Motameny, S., Wonczak, S., Thiele, H., Nieroda, L., Jabbari, K., Borowski, S., Sinha, V., Gunia, W., Lang, U., Achter, V., and Nürnberg, P. (2015) Leveraging the power of high performance computing for next generation sequencing data analysis: tricks and twists from a high throughput exome workflow. *PLoS One* **10**, e0126321
22. Elsayed, S. M., Phillips, J. B., Heller, R., Thoenes, M., Elsobky, E., Nürnberg, G., Nürnberg, P., Seland, S., Ebermann, I., Altmüller, J., Thiele, H., Toliat, M., Körber, F., Hu, X. J., Wu, Y. D., Zaki, M. S., Abdel-Salam, G., Gleeson, J., Boltshauser, E., Westerfield, M., and Bolz, H. J. (2015) Non-manifesting AHI1 truncations indicate localized loss-of-function tolerance in a severe Mendelian disease gene. *Hum. Mol. Genet.* **24**, 2594–2603
23. Beck, B. B., Phillips, J. B., Bartram, M. P., Wegner, J., Thoenes, M., Pannes, A., Sampson, J., Heller, R., Göbel, H., Koerber, F., Neugebauer, A., Hedergott, A., Nürnberg, G., Nürnberg, P., Thiele, H., Altmüller, J., Toliat, M. R., Staubach, S., Boycott, K. M., Valente, E. M., Janecke, A. R., Eisenberger, T., Bergmann, C., Tebbe, L., Wang, Y., Wu, Y., Fry, A. M., Westerfield, M., Wolfrum, U., and Bolz, H. J. (2014) Mutation of POC1B in a severe syndromic retinal ciliopathy. *Hum. Mutat.* **35**, 1153–1162
24. Lek, M., Karczewski, K. J., Minikel, E. V., Samocha, K. E., Banks, E., Fennell, T., O'Donnell-Luria, A. H., Ware, J. S., Hill, A. J., Cummings, B. B., Tukiainen, T., Birnbaum, D. P., Kosmicki, J. A., Duncan, L. E., Estrada, K., Zhao, F., Zou, J., Pierce-Hoffman, E., Berghout, J.,

Cooper, D. N., Deflaux, N., DePristo, M., Do, R., Flannick, J., Fromer, M., Gauthier, L., Goldstein, J., Gupta, N., Howrigan, D., Kiezun, A., Kurki, M. I., Moonshine, A. L., Natarajan, P., Orozco, L., Peloso, G. M., Poplin, R., Rivas, M. A., Ruano-Rubio, V., Rose, S. A., Ruderfer, D. M., Shakir, K., Stenson, P. D., Stevens, C., Thomas, B. P., Tiao, G., Tusie-Luna, M. T., Weisburd, B., Won, H. H., Yu, D., Altshuler, D. M., Ardissino, D., Boehnke, M., Danesh, J., Donnelly, S., Elosua, R., Florez, J. C., Gabriel, S. B., Getz, G., Glatt, S. J., Hultman, C. M., Kathiresan, S., Laakso, M., McCarroll, S., McCarthy, M. I., McGovern, D., McPherson, R., Neale, B. M., Palotie, A., Purcell, S. M., Saleheen, D., Scharf, J. M., Sklar, P., Sullivan, P. F., Tuomilehto, J., Tsuang, M. T., Watkins, H. C., Wilson, J. G., Daly, M. J., and MacArthur, D. G.; Exome Aggregation Consortium. (2016) Analysis of protein-coding genetic variation in 60,706 humans. *Nature* **536**, 285–291

25. Görg, B., Karababa, A., Shafigullina, A., Bidmon, H. J., and Häussinger, D. (2015) Ammonia-induced senescence in cultured rat astrocytes and in human cerebral cortex in hepatic encephalopathy. *Glia* **63**, 37–50
26. Gan, W., Liu, X. L., Yu, T., Zou, Y. G., Li, T. T., Wang, S., Deng, J., Wang, L. L., and Cai, J. P. (2018) Urinary 8-oxo-7,8-dihydroguanosine as a potential biomarker of aging. *Front. Aging Neurosci.* **10**, 34
27. García-Cañaveras, J. C., Donato, M. T., Castell, J. V., and Lahoz, A. (2012) Targeted profiling of circulating and hepatic bile acids in human, mouse, and rat using a UPLC-MRM-MS-validated method. *J. Lipid Res.* **53**, 2231–2241
28. Provencher, S. W. (1993) Estimation of metabolite concentrations from localized in vivo proton NMR spectra. *Magn. Reson. Med.* **30**, 672–679
29. Wilson, M., Reynolds, G., Kauppinen, R. A., Arvanitis, T. N., and Peet, A. C. (2011) A constrained least-squares approach to the automated quantitation of in vivo ^{1}H magnetic resonance spectroscopy data. *Magn. Reson. Med.* **65**, 1–12
30. Penmatsa, A., Wang, K. H., and Gouaux, E. (2013) X-ray structure of dopamine transporter elucidates antidepressant mechanism. *Nature* **503**, 85–90
31. Jorgensen, W. L., Chandrasekhar, J., Madura, J. D., Impey, R. W., and Klein, M. L. (1983) Comparison of simple potential functions for simulating liquid water. *J. Chem. Phys.* **79**, 926–935
32. Le Grand, S., Götz, A. W., and Walker, R. C. (2013) SPFP: speed without compromise-A mixed precision model for GPU accelerated molecular dynamics simulations. *Comput. Phys. Commun.* **184**, 374–380
33. Case, D. A., Walker, R. C., Cheatham III, T. E., Simmerling, C. L., Roitberg, A. E., Merz, K. M., Luo, R., Darden, T. A., Wang, J., Duke, R. E., Roe, D. R., Le Grand, S., Swails, J. M., Götz, A. W., Smith, J., Cerutti, D. S., Brozell, S. R., Luchko, T., Cruzeiro, V. W., Ghoreishi, D., Monard, G., Sagui, C., Pan, F., Andrés, C. G., Miao, Y., Shen, J., Harris, R., Lin, C., Mermelstein, D. J., Li, P., Onufriev, A., Izadi, S., Wolf, R. M., Wu, X., Gohlke, H., Schott-Verdugo, S., Homeyer, N., Qi, R., Xiao, L., Wei, H., Greene, D. A., Lee, T.-S., York, D. M., Liu, J., Nguyen, H., Omelyan, I., Kovalenko, A., and Kollman, P. A. (2018) *AMBER 2018*, University of California, San Francisco, CA, USA
34. Pfleger, C., Rathi, P. C., Klein, D. L., Radestock, S., and Gohlke, H. (2013) Constraint Network Analysis (CNA): a Python software package for efficiently linking biomacromolecular structure, flexibility, (thermo-)stability, and function. *J. Chem. Inf. Model.* **53**, 1007–1015
35. Pfleger, C., Minges, A., Boehm, M., McClendon, C. L., Torella, R., and Gohlke, H. (2017) Ensemble- and rigidity theory-based perturbation approach to analyze dynamic allostery. *J. Chem. Theory Comput.* **13**, 6343–6357
36. Biasini, M., Bienert, S., Waterhouse, A., Arnold, K., Studer, G., Schmidt, T., Kiefer, F., Gallo Cassarino, T., Bertoni, M., Bordoli, L., and Schwede, T. (2014) SWISS-MODEL: modelling protein tertiary and quaternary structure using evolutionary information. *Nucleic Acids Res.* **42** (Web Server issue), W252–W258
37. Chen, V. B., Arendall III, W. B., Headd, J. J., Keedy, D. A., Immormino, R. M., Kapral, G. J., Murray, L. W., Richardson, J. S., and Richardson, D. C. (2010) MolProbity: all-atom structure validation for macromolecular crystallography. *Acta Crystallogr. D Biol. Crystallogr.* **66**, 12–21
38. Forrest, L. R., Tang, C. L., and Honig, B. (2006) On the accuracy of homology modeling and sequence alignment methods applied to membrane proteins. *Biophys. J.* **91**, 508–517
39. Yamashita, A., Singh, S. K., Kawate, T., Jin, Y., and Gouaux, E. (2005) Crystal structure of a bacterial homologue of Na+/Cl–dependent neurotransmitter transporters. *Nature* **437**, 215–223
40. Jo, S., Kim, T., Iyer, V. G., and Im, W. (2008) CHARMM-GUI: a web-based graphical user interface for CHARMM. *J. Comput. Chem.* **29**, 1859–1865
41. Wu, E. L., Cheng, X., Jo, S., Rui, H., Song, K. C., Dávila-Contreras, E. M., Qi, Y., Lee, J., Monje-Galvan, V., Venable, R. M., Klauda, J. B., and Im, W. (2014) CHARMM-GUI membrane builder toward realistic biological membrane simulations. *J. Comput. Chem.* **35**, 1997–2004
42. Pastor, R. W., Brooks, B. R., and Szabo, A. (1988) An analysis of the accuracy of Langevin and molecular-dynamics algorithms. *Mol. Phys.* **65**, 1409–1419
43. Loncharich, R. J., Brooks, B. R., and Pastor, R. W. (1992) Langevin dynamics of peptides: the frictional dependence of isomerization rates of N-acetylalanyl-N'-methylamide. *Biopolymers* **32**, 523–535
44. Ryckaert, J.-P., Ciccotti, G., and Berendsen, H. J. C. (1977) Numerical integration of the cartesian equations of motion of a system with constraints: molecular dynamics of n-alkanes. *J. Comput. Phys.* **23**, 327–341
45. Darden, T. A., York, D. M., and Pedersen, L. (1993) Particle mesh Ewald - an N·Log(N) method for Ewald sums in large systems. *J. Chem. Phys.* **98**, 10089–10092
46. Shimamura, T., Weyand, S., Beckstein, O., Rutherford, N. G., Hadden, J. M., Sharples, D., Sansom, M. S. P., Iwata, S., Henderson, P. J. F., and Cameron, A. D. (2010) Molecular basis of alternating access membrane transport by the sodium-hydantoin transporter Mhp1. *Science* **328**, 470–473
47. Watanabe, A., Choe, S., Chaptal, V., Rosenberg, J. M., Wright, E. M., Grabe, M., and Abramson, J. (2010) The mechanism of sodium and substrate release from the binding pocket of vSGLT. *Nature* **468**, 988–991
48. Venable, R. M., Brown, F. L. H., and Pastor, R. W. (2015) Mechanical properties of lipid bilayers from molecular dynamics simulation. *Chem. Phys. Lipids* **192**, 60–74
49. Chavent, M., Duncan, A. L., and Sansom, M. S. P. (2016) Molecular dynamics simulations of membrane proteins and their interactions: from nanoscale to mesoscale. *Curr. Opin. Struct. Biol.* **40**, 8–16
50. Dickson, C. J., Madej, B. D., Skjevik, Å. A., Betz, R. M., Teigen, K., Gould, I. R., and Walker, R. C. (2014) Lipid14: the amber lipid force field. *J. Chem. Theory Comput.* **10**, 865–879
51. Maier, J. A., Martinez, C., Kasavajhala, K., Wickstrom, L., Hauser, K. E., and Simmerling, C. (2015) ff14SB: improving the accuracy of protein side chain and backbone parameters from ff99SB. *J. Chem. Theory Comput.* **11**, 3696–3713
52. Pagani, G., and Gohlke, H. (2018) On the contributing role of the transmembrane domain for subunit-specific sensitivity of integrin activation. *Sci. Rep.* **8**, 5733
53. Otte, M., Schweinitz, A., Bonus, M., Enke, U., Schumann, C., Gohlke, H., and Benndorf, K. (2018) Hydrophobic alkyl chains substituted to the 8-position of cyclic nucleotides enhance activation of CNG and HCN channels by an intricate enthalpy - entropy compensation. *Sci. Rep.* **8**, 14960
54. Galindo-Murillo, R., Roe, D. R., and Cheatham III, T. E. (2015) Convergence and reproducibility in molecular dynamics simulations of the DNA duplex d(GCACGAACGAACGAACGC). *Biochim. Biophys. Acta* **1850**, 1041–1058
55. Roe, D. R., and Cheatham III, T. E. (2013) PTRAJ and CPPTRAJ: software for processing and analysis of molecular dynamics trajectory data. *J. Chem. Theory Comput.* **9**, 3084–3095
56. Hermans, S. M. A., Pfleger, C., Nutschel, C., Hanke, C. A., and Gohlke, H. (2017) Rigidity theory for biomolecules: concepts, software, and applications. *Wiley Interdiscip. Rev. Comput. Mol. Sci.* **7**, e1311
57. Jacobs, D. J., and Hendrickson, B. (1997) An algorithm for two-dimensional rigidity percolation: the pebble game. *J. Comput. Phys.* **137**, 346–365
58. Moukarzel, C., and Duxbury, P. M. (1999) Comparison of rigidity and connectivity percolation in two dimensions. *Phys. Rev. E Stat. Phys. Plasmas Fluids Relat. Interdiscip. Topics* **59**, 2614–2622
59. Jacobs, D. J., Rader, A. J., Kuhn, L. A., and Thorpe, M. F. (2001) Protein flexibility predictions using graph theory. *Proteins* **44**, 150–165
60. Dahiyat, B. I., Gordon, D. B., and Mayo, S. L. (1997) Automated design of the surface positions of protein helices. *Protein Sci.* **6**, 1333–1337
61. Rader, A. J., Hespenheide, B. M., Kuhn, L. A., and Thorpe, M. F. (2002) Protein unfolding: rigidity lost. *Proc. Natl. Acad. Sci. USA* **99**, 3540–3545
62. Radestock, S., and Gohlke, H. (2008) Exploiting the link between protein rigidity and thermostability for data-driven protein engineering. *Eng. Life Sci.* **8**, 507–522
63. Rader, A. J. (2009) Thermostability in rubredoxin and its relationship to mechanical rigidity. *Phys. Biol.* **7**, 16002

64. Hespenheide, B. M., Rader, A. J., Thorpe, M. F., and Kuhn, L. A. (2002) Identifying protein folding cores from the evolution of flexible regions during unfolding. *J. Mol. Graph. Model.* **21**, 195–207
65. Rathi, P. C., Jaeger, K.-E., and Gohlke, H. (2015) Structural rigidity and protein thermostability in variants of lipase a from Bacillus subtilis. *PLoS One* **10**, e0130289
66. Skolnick, J., Jaroszewski, L., Kolinski, A., and Godzik, A. (1997) Derivation and testing of pair potentials for protein folding. When is the quasichemical approximation correct? *Protein Sci.* **6**, 676–688
67. Imaki, H., Jacobson, S. G., Kemp, C. M., Knighton, R. W., Neuringer, M., and Sturman, J. (1993) Retinal morphology and visual pigment levels in 6- and 12-month-old rhesus monkeys fed a taurine-free human infant formula. *J. Neurosci. Res.* **36**, 290–304
68. Imaki, H., Neuringer, M., and Sturman, J. (1996) Long-term effects on retina of rhesus monkeys fed taurine-free human infant formula. *Adv. Exp. Med. Biol.* **403**, 351–360
69. Froger, N., Jammoul, F., Gaucher, D., Cadetti, L., Lorach, H., Degardin, J., Pain, D., Dubus, E., Forster, V., Ivkovic, I., Simonutti, M., Sahel, J. A., and Picaud, S. (2013) Taurine is a crucial factor to preserve retinal ganglion cell survival. *Adv. Exp. Med. Biol.* **775**, 69–83
70. Wakeling, M. N., Laver, T. W., Wright, C. F., De Franco, E., Stals, K. L., Patch, A. M., Hattersley, A. T., Flanagan, S. E., Ellard, S., and Study, D. D. D. (2018) Homozygosity mapping provides supporting evidence of pathogenicity in recessive Mendelian disease. *Genet. Med.* **21**, 982–986; erratum: 21, 766
71. Kantcheva, A. K., Quick, M., Shi, L., Winther, A. M., Stolzenberg, S., Weinstein, H., Javitch, J. A., and Nissen, P. (2013) Chloride binding site of neurotransmitter sodium symporters. *Proc. Natl. Acad. Sci. USA* **110**, 8489–8494
72. Rascher, K., Servos, G., Berthold, G., Hartwig, H. G., Warskulat, U., Heller-Stilb, B., and Häussinger, D. (2004) Light deprivation slows but does not prevent the loss of photoreceptors in taurine transporter knockout mice. *Vision Res.* **44**, 2091–2100
73. Farrar, G. J., Carrigan, M., Dockery, A., Millington-Ward, S., Palfi, A., Chadderton, N., Humphries, M., Kiang, A. S., Kenna, P. F., and Humphries, P. (2017) Toward an elucidation of the molecular genetics of inherited retinal degenerations. *Hum. Mol. Genet.* **26**, R2–R11
74. Pierce, E. A., and Bennett, J. (2015) The status of RPE65 gene therapy trials: safety and efficacy. *Cold Spring Harb. Perspect. Med.* **5**, a017285
75. Scholl, H. P., Strauss, R. W., Singh, M. S., Dalkara, D., Roska, B., Picaud, S., and Sahel, J. A. (2016) Emerging therapies for inherited retinal degeneration. *Sci. Transl. Med.* **8**, 368rv6
76. Behnen, P., Felline, A., Comitato, A., Di Salvo, M. T., Raimondi, F., Gulati, S., Kahremany, S., Palczewski, K., Marigo, V., and Fanelli, F. (2018) A small chaperone improves folding and routing of rhodopsin mutants linked to inherited blindness. *Science* **4**, 1–19
77. Alagramam, K. N., Gopal, S. R., Geng, R., Chen, D. H., Nemet, I., Lee, R., Tian, G., Miyagi, M., Malagu, K. F., Lock, C. J., Esmieu, W. R., Owens, A. P., Lindsay, N. A., Ouwehand, K., Albertus, F., Fischer, D. F., Bürli, R. W., MacLeod, A. M., Harte, W. E., Palczewski, K., and Imanishi, Y. (2016) A small molecule mitigates hearing loss in a mouse model of Usher syndrome III. *Nat. Chem. Biol.* **12**, 444–451

Received for publication April 8, 2019.
Accepted for publication July 1, 2019.